

T Tauri stars in the SuperWASP and NSVS surveys [★]

Ľ. Hambálek^{1†}, M. Vaňko¹, E. Paunzen², B. Smalley³

¹*Astronomical Institute, Slovak Academy of Sciences, 059 60 Tatranská Lomnica, Slovakia*

²*Department of Theoretical Physics and Astrophysics, Masaryk University, Kotlářská 2, 61137 Brno, Czech Republic*

³*Astrophysics Group, Keele University, Keele ST5 5BG, UK*

Accepted 2018 February 28. Received 2018 January 19; in original form 2017 December 14

ABSTRACT

We present a study of the long-term optical variability of young T Tauri stars using previously unpublished data from the SuperWASP project. Other publicly available photometry from NSVS and the NASA K2 mission were used to check and supplement our results. Our sample includes twenty weak-lined T Tauri stars in the Taurus-Auriga star-forming region. We have performed a period search on the long time-series photometry and derived the mean periods of stars in our sample. We have found new periods for the stars V1334 Tau (HD 283782) and V1349 Tau (HD 31281) without any period estimation in literature. The rotation period was found for the primary star in the binary V773 Tau (HD 283447). Several earlier results were updated. For the star V410 Tau (HD 283518), we have compared the light curve changes found in previous studies to the new measurements, and attributed the evolution of spots to a ~ 15 -year cycle similar to the solar 11-year cycle. We have also derived luminosities and effective temperatures for our targets, in order to locate them in the Hertzsprung-Russell diagram and to calibrate the masses and ages of the target stars.

Key words: stars: variables: T Tauri, Herbig Ae/Be

1 INTRODUCTION

The kinematic association of many T Tauri stars with dark clouds where stars are formed (Herbig 1977), and the presence of Li I $\lambda 6707$ Å in absorption (Bertout 1989) show that T Tauri stars are young stellar objects. They have low or intermediate masses ($0.5\text{--}2.5 M_{\odot}$) and are defined as pre-main-sequence (PMS) stars that are surrounded by a nebula and show emission lines in their spectra (Joy 1945). These objects typically have spectral types ranging from G to M. PMS models show that their interiors are either fully convective or possess outer convective envelopes, depending on the age and mass of the star (Hussain 2012). The properties of these PMS objects were reviewed by, e.g. Menard & Bertout (1999) who emphasized two subgroups; the so-called “classical” T Tauri stars (CTTS), still actively accreting from their circumstellar disks and the “weak-line” T Tauri stars (WTTS), no longer surrounded by a circumstellar disk.

Depending on their spectral type, T Tauri stars can have ages ranging from less than one to tens of Myr. Comparing the position of these stars in the HR diagram with theoretical evolutionary tracks (D’Antona & Mazitelli 1994; Swenson et al. 1994) gives an upper-limit to the estimated

age of the stars. However, these evolutionary tracks do not take into account accretion and Siess, Forestini & Bertout (1997), show that they underestimate ages by a factor of 2 to 3.

Ubiquitous amongst T Tauri stars is their variability. As was already noticed in the original definition by Joy (1945), the prototype T Tauri exhibits strong and mostly irregular variability on time-scales from hours to months and even years. This is true for the broad-band photometry at all wavelengths (radio to X-ray). On top of a periodic signal due to star spots, modulated by stellar rotation, the reason for this type of variability is stellar youth, apparent through strong magnetic activity and variable accretion and/or extinction (Herbst et al. 1994). Variations are not restricted to photometric observations. Emission lines are also changing in intensity and shape (e.g., Johns & Basri 1995; Lago & Gameiro 1998), and polarimetric studies imply variations in the degree and position angle of polarization as well (Appenzeller & Mundt 1989).

There have been many previous photometric surveys in the optical and infrared. We refrain from presenting a comprehensive overview here, but mention several of the surveys that have studied the photometric variability of our target stars. Bouvier et al. (1997) observed in the optical range 58 WTTS which were detected in the ROSAT All-Sky Survey (RASS). They were able to derive rotational

[★] Based on the data from SuperWASP and NSVS archives.

[†] lhambalek@ta3.sk

periods for 18 of their stars, all but one being ascribed to rotational modulation by stellar spots. Grankin et al. (2008) presented a homogeneous set of photometric measurements for WTTS extending for up to 20 years. Their data were collected within the framework of the ROTOR (Research Of Traces Of Rotation) program, aimed at the study of the photometric variability of PMS objects. The data set contains rotational periods for 35 out of 48 stars. Further optical photometry, including the behaviour on time-scales over more than several years, has been studied in the works of Gahm et al. (1993), Grankin et al. (2007), Percy et al. (2010), and Ibryamov et al. (2015).

Recently, Rigon et al. (2017) presented a study, including long-term variability of CTTS (mostly in the Taurus-Auriga region), based on data from the Wide Angle Search for Planets (SuperWASP). They found that the overwhelming majority of CTTS have a low-level variability with $\sigma < 0.3$ mag dominated by time-scales of a few weeks, consistent with rotational modulation. The presence of long-term variability correlates with the spectral slope at $3\text{--}5\ \mu\text{m}$, which is an indicator of inner disc geometry, and with the $U - B$ band slope, which is an accretion diagnostics. This shows that the long-term variations in CTTS are predominantly driven by processes in the inner disc and in the accretion zone.

The extensive simultaneous multiwavelength studies of Carpenter et al. 2001 find that the bulk of T Tauri stars show photometric variability on the order of 0.2 magnitudes in *JHKs* and ~ 0.5 mag in their respective near-infrared (NIR) colours. Further characterization in NIR was studied by, e.g. Eiroa et al. (2002), Alves de Oliveira & Casali (2008), Rice et al. (2012). The photometric properties have been extended to the mid-infrared (Flaherty et al. 2012; Rebull et al. 2014) and to the far-infrared by (Billot et al. 2012).

The most advanced survey of T Tauri stars to-date is the Coordinated Synoptic Investigation's study of the NGC 2264 star-forming region (CSI 2264) (Cody et al. 2014). The multi-wavelength observation campaign utilized 16 telescopes, including the space-based observatories CoRoT and Spitzer. Their unprecedented photometric precision $\leq 1\%$ and a cadence down to several minutes sets a new standard for this kind of surveys. Cody et al. 2014; Stauffer et al. 2015; McGinnis et al. 2015 show that young-star variability can be caused not only by cold spots, but also by circumstellar obscuration events, hot spots on the star and/or disk, accretion bursts, and rapid structural changes in the inner disk.

The main goal of our study is to extend the knowledge of T Tauri stars by analysing several years of high-cadence monitoring of twenty WTTS using the data from SuperWASP and NSVS surveys. Our particular emphasis is to search for possible evolution in the long-term variability of brightness changes caused by the presence of spots.

2 TARGET SELECTION

We have found that many bona fide T Tauri stars (originally designated as members of Tau-Aur region) in publications listed in Table 1 are without reliable periods of photometric variability and/or physical parameters. We ex-

cluded any known CTTS and stars with close visual companions from the list. Furthermore, we selected only stars with $V < 11$ mag, as this is the brightness limit for spectroscopic follow-up observations at Stará Lesná observatory (Pribulla et al. 2015). We arrived to a sample of twenty WTTS. All the targets have been observed by our own spectroscopic survey and the EW of Li $\lambda 6707$ line was measured to confirm the evolutionary status of targets. Patterer et al. (1993) found for HD 283518 (V410 Tau) $\text{EW}(\text{Li}) = 0.547 \pm 0.084\ \text{\AA}$. All other stars in our sample had their EWs measured in range of $0.165 - 0.472\ \text{\AA}$.

2.1 Evolution stage of target stars

For the analysis of the evolutionary status of a star, the effective temperature and luminosity is needed to locate the object in the Hertzsprung-Russell-diagram (HRD). Then, the age and mass can be deduced from corresponding isochrones.

Only stars with an available parallax from the *Gaia* DR2 (Lindgren et al. 2018) or earlier TGAS catalogue (Michalik et al. 1993) were included in this analysis. We have used parallax from TGAS only for HD 286178, since the value is missing in the newer *Gaia* DR2 catalogue. However, based on its distance, HD 286178 may not be a member of the Taurus-Auriga SFR. For HD 283782, the *Gaia* DR2 found two astrometric positions separated by only 1.9 arcsec. We have used the parallax of the brighter (in *Gaia* G band) target, closer to RA_{2000} , Dec_{2000} of HD 283782. No parallax was available for star HD 284135.

The calculation of luminosity is based on the parallax (or distance), apparent magnitude, reddening and bolometric correction (BC). Within the *Gaia* and *Hipparcos* era, we now have quite accurate parallaxes for stars in the solar vicinity, where also our targets are located. The estimation of reddening, especially in denser areas such as the Taurus-Auriga region, still poses several problems and limitations. One way out of the dilemma could be reddening maps (Schlafly et al. 2014). However, their resolutions are not sufficient for our purpose. We therefore used another approach, by taking available reddening estimates from the literature (Meištas & Straišys 1981; Chavarría-K et al. 2000; Grankin 2013; Herczeg & Hillenbrand 2014) and the dereddening method based on the Strömgren-Crawford *uvby* β photometric system (Crawford 1975; Schuster & Nissen 1989). The *uvby* β photometric data were taken from Paunzen (2015). An unweighted mean and its error on A_V was calculated (Table 2). The values for A_V range up to 1.10 mag with a mean of the error of 0.13 mag. These values agree with that expected in this region of the sky. However, the uncertainties are the largest contribution to the overall error in $\log L/L_\odot$. The BC, especially derived for PMS stars, were taken from Pecaú & Mamajek (2014).

The apparent magnitudes are from Grankin (2013), except for HD 30171, HD 283447, HD 283798, and HD 283518 which are not included in this reference. For these stars, we have used values from the AAVSO Photometric All-Sky Survey (APASS), after checking the magnitudes in common with Grankin (2013), which yielded an excellent agreement. For the final error estimation in $\log L/L_\odot$, we applied full propagation of uncertainties for all the measurements.

A careful assessment of the literature about effective temperature estimation of T Tauri stars revealed that there

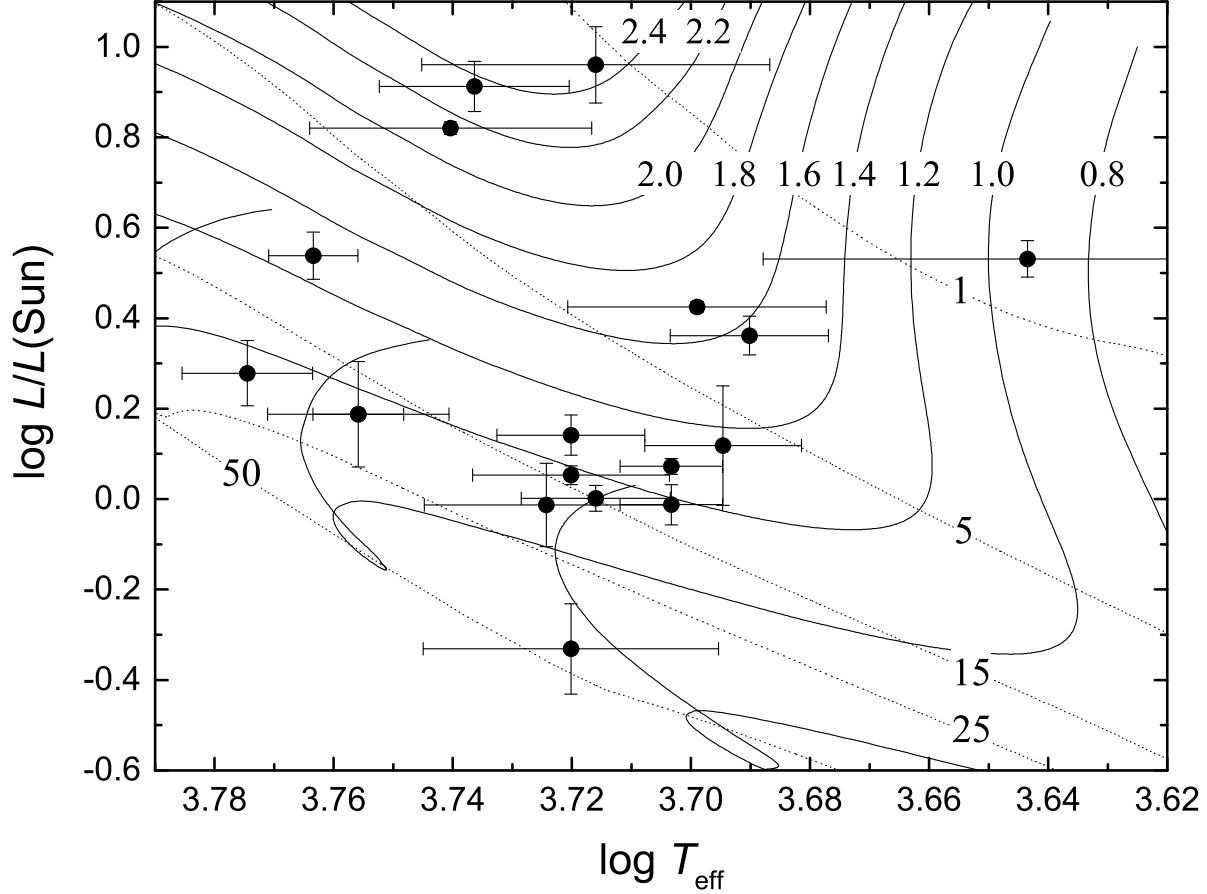
Table 1. The basic characteristic of the selected targets. Distances are calculated from parallaxes from the *Gaia* DR2 (Lindegren et al. 2018) catalogue. Distance of HD 286178 is from TGAS (Michalik et al. 1993). NSVS IDs with “?” are close to another target and may have been misidentified.

Object	SuperWASP ID NSVS ID	R.A. (2000)	DEC (2000)	V_{mag}	Sp. type	P [d]	Dist. [pc]	Refer.
HD 285281	1SWASPJ040031.06+193520.8 9414189?	04 00 31.07	19 35 20.8	10.17	K1	1.1683	$135.3^{+1.2}_{-1.2}$	(1)(2)(6)
BD+19 656	1SWASPJ040519.59+200925.5 9417695?	04 05 19.61	20 09 25.2	10.12	K1	2.86 (0.741)	$108.5^{+0.7}_{-0.7}$	(2)(3)(6)
HD 284135	1SWASPJ040540.58+224812.0 6750588	04 05 40.58	22 48 12.0	09.39	G3V	0.8160	–	(1)(6)
HD 284149	1SWASPJ040638.08+201811.1 9418722	04 06 38.80	20 18 11.2	09.63	G0	1.0790	$118.2^{+0.7}_{-0.7}$	(1)(2)(4)(6)
HD 281691	1SWASPJ040909.74+290130.2 6754307	04 09 09.74	29 01 30.3	10.68	G8III	2.74?	$110.3^{+0.5}_{-0.5}$	(1)(6)
HD 284266	1SWASPJ041522.91+204417.0 9425183	04 15 22.92	20 44 16.9	10.51	K0V	1.83	$119.9^{+1.0}_{-1.0}$	(1)(2)(6)
HD 284503	1SWASPJ043049.18+211410.6 9436598	04 30 49.19	21 14 10.7	10.24	G8	0.736	$111.6^{+0.7}_{-0.7}$	(1)(6)
HD 284496	1SWASPJ043116.85+215025.2 9444066?	04 31 16.86	21 50 25.3	10.80	K0	2.71	$125.8^{+0.6}_{-0.6}$	(1)(5)
HD 285840	1SWASPJ043242.43+185510.2 9444857?	04 32 42.43	18 55 10.2	10.85	K1V	1.55	$90.5^{+0.3}_{-0.3}$	(2)(5)(6)
HD 285957	1SWASPJ043839.06+154613.6 9449108	04 38 39.07	15 46 13.6	10.86	K1	3.07	$139.2^{+1.1}_{-1.1}$	(2)(5)(6)
HD 283798	1SWASPJ044155.15+265849.4 6778011	04 41 55.16	26 58 49.4	09.55	G7	0.6?	$110.8^{+0.6}_{-0.6}$	(1)(2)(6)
HD 283782	1SWASPJ044454.45+271745.2 6780256	04 44 54.40	27 17 45.5	09.48	K1	?	$168.0^{+6.8}_{-6.3}$	(1)(2)(6)
HD 30171	1SWASPJ044551.29+155549.7 9455701	04 45 51.30	15 55 49.7	09.36	G5	1.104	$184.9^{+3.9}_{-3.7}$	(2)(5)(6)
HD 31281	1SWASPJ045509.62+182631.1 no data	04 55 09.62	18 26 31.1	09.14	G1	?	$122.4^{+0.6}_{-0.6}$	(1)(2)(6)
HD 286179	1SWASPJ045700.64+151753.1 9466913	04 57 00.65	15 17 53.1	10.39	G3	3.33	$123.7^{+1.0}_{-1.0}$	(5)(6)
HD 286178	1SWASPJ045717.65+152509.4 9467195	04 57 17.66	15 25 09.5	10.54	K1	2.39	$74.3^{+3.5}_{-3.2}$	(2)(5)(6)
HD 283447	1SWASPJ041412.91+281212.3 6758228	04 14 12.92	28 12 12.3	10.68	K3V	51	$128.1^{+2.3}_{-2.3}$	(8)
HD 283572	1SWASPJ042158.84+281806.4 no data	04 21 58.85	28 18 06.5	09.03	G5	1.529	$130.3^{+0.9}_{-0.9}$	(1)(2)
HD 285778	1SWASPJ042710.57+175042.6 9440985	04 27 10.57	17 50 42.6	10.22	K1	2.734	$120.1^{+0.8}_{-0.8}$	(7)
HD 283518	1SWASPJ041831.10+282716.0 6761377	04 18 31.12	28 27 16.1	10.75	K3V	1.87	$130.4^{+0.9}_{-0.9}$	(1)(9)(10)

References: (1) Grankin (2013), (2) Daemgen et al. (2015), (3) Grankin, Artemenko & Melnikov (2007), (4) Bonavita et al. (2014), (5) Bouvier et al. (1997), (6) Wichmann et al. (2000), (7) Grankin et al. (2008), (8) Welty (1995), (9) Stelzer et al. (2003), and (10) Fernández et al. (2004)

Table 2. The astrophysical parameters of our targets with available parallax measurements.

Object	A_V	$\log T_{\text{eff}}$	BC_V	$\log L/L_\odot$	$M [M_\odot]$	age [Myr]
HD 285281	0.47(2)	3.699(22)	-0.27	+0.43(1)	1.4 – 1.7	1 – 8
BD+19 656	0.27(4)	3.703(9)	-0.26	+0.07(2)	1.2 – 1.3	7 – 12
HD 284149	0.19(18)	3.775(11)	-0.04	+0.28(5)	1.0 – 1.2	15 – 25
HD 281691	0.19(11)	3.703(9)	-0.26	-0.01(4)	1.1 – 1.3	8 – 18
HD 284266	0.16(23)	3.724(20)	-0.18	-0.01(9)	1.0 – 1.2	15 – 30
HD 284503	0.19(5)	3.720(17)	-0.19	+0.05(2)	1.1 – 1.3	10 – 20
HD 284496	0.21(7)	3.716(13)	-0.21	+0.00(3)	1.1 – 1.2	12 – 20
HD 285840	0.17(25)	3.720(25)	-0.19	-0.33(10)	0.8 – 1.0	20 – 70
HD 285957	0.27(33)	3.695(13)	-0.29	+0.12(13)	1.2 – 1.5	3 – 13
HD 283798	0.00(1)	3.756(8)	-0.09	+0.19(1)	0.9 – 1.3	17 – 21
HD 283782	0.63(19)	3.716(29)	-0.21	+0.96(18)	1.8 – 2.7	< 3
HD 30171	0.36(13)	3.736(16)	-0.15	+0.91(6)	2.1 – 2.5	2 – 4
HD 31281	0.26(13)	3.763(7)	-0.06	+0.54(5)	1.4 – 1.6	8 – 12
HD 286179	0.44(29)	3.756(15)	-0.09	+0.19(12)	1.1 – 1.4	10 – 35
HD 283447	0.95(10)	3.690(13)	-0.30	+0.36(4)	1.4 – 1.7	2 – 4
HD 283518	1.10(10)	3.643(44)	-0.60	+0.53(4)	0.5 – 1.6	< 2
HD 283572	0.48(3)	3.740(24)	-0.14	+0.82(1)	1.8 – 2.5	2 – 5
HD 285778	0.15(11)	3.720(12)	-0.19	+0.14(4)	1.2 – 1.4	8 – 15

**Figure 1.** Location of the target stars in the $\log T_{\text{eff}}$ versus $\log L/L_\odot$ diagram together with the PMS evolutionary tracks (solid curves) and isochrones (dotted curves) based on the Pisa Stellar Models (Tognelli et al. 2011). The evolutionary tracks range from 2.4 to $0.8 M_\odot$ and isochrones from 1 to 50 Myr, as indicated.

are significant differences in the values for individual stars. These are caused by the usage of different stellar atmospheres, spectral resolution, analytic methods and so on. An excellent example of the challenges to be faced is shown by Lebzelter et al. (2012) for the case of cool type Giants. As for reddening, no homogeneous source was found. We therefore calculated unweighted means of values from the literature (Palla & Stahler 2002; Ammons et al. 2006; Wright et al. 2011; Grankin 2013; Davies et al. 2014; McDonald et al. 2017) and the Strömgren-Crawford *uvby* β calibration of (Napiwotzki et al. 1993). The latter is based on the β index which is an excellent indicator for the $\log T_{\text{eff}}$. The combination of a narrow and wide filter centred at H β guarantees that any possible emission has no significant effect. The final uncertainties are between 100 and 450 K, respectively. In Table 2 all the derived astrophysical parameters with their uncertainties are listed.

Finally, we used PMS evolutionary tracks based on the Pisa Stellar Models (Tognelli et al. 2011) to investigate the evolutionary status of our targets. The evolutionary tracks with $[X, Y, Z]$ of $[0.609, 0.2533, 0.1377]$, i.e. solar metallicity, were used. In Fig. 1, the location of the target stars in the $\log T_{\text{eff}}$ versus $\log L/L_{\odot}$ diagram is shown. The error bars were used to determine the extent of the possible masses and ages (also in Table 2) of candidate stars in comparison to Pisa Stellar Model isochrones. We have found that the stars in our sample should be younger than at most 70 Myr. This is close to, or inclusive of, the 10–100 Myr interval for the post T Tauri stars (PTTS) defined by Jensen (2001). The uncertainties, mainly due to effective temperature, allow for the estimating of masses to within the range $\pm 0.1 M_{\odot}$ to $\pm 0.2 M_{\odot}$. To make a comprehensive analysis of the correlation between rotational period and evolutionary status of our targets, more precise and homogeneous effective temperatures are required.

3 PHOTOMETRIC DATA

For the determination of periods, we needed light curves measured during long observation campaigns, which are best taken with the same instrument and reduced with the same pipeline. There are several public data available, notably the SuperWASP database. With our access to all of the data presently kept in the SuperWASP archives, we have based our photometric light-curve investigation on almost 8 years of observations. The separation into observing seasons is a natural one, since the target region was best observable from autumn to spring. To expand our time-domain, we have also added photometry from the NSVS archive. For ten targets we have found photometry provided by the Kepler *K2* mission. We break down the individual observing seasons in Table 3.

3.1 SuperWASP data

The WASP instruments have been described by Pollacco et al. (2006), and the reduction techniques discussed by Smalley et al. (2011) and Holdsworth et al. (2014). The aperture-extracted photometry from each camera on each night was corrected for atmospheric extinction, instrumental colour response, and system zero-point

relative to a network of local secondary standards. The resulting pseudo- V magnitudes are comparable to *Tycho-2* (Høg et al. 2000) V magnitudes (Butters et al. 2010). In this paper, we have used so far publicly unavailable SuperWASP data provided by our co-author B. Smalley.

The SuperWASP data were gathered from July 2004 to January 2012, covering 7 observing seasons in total. The mean season duration is 143 days, however, season 3 consists of only 12 days. Usually we had five different seasons available for our targets. For the star HD 31281 we found only two seasons of useful data in the archive. The mean cadence of observations is ~ 80 seconds.

For all targets, the SuperWASP archive provides 417 603 points in total and typically ~ 4000 points per object in each season. The SuperWASP pre-clean procedure includes the following steps: (i) keeping data with errors of < 0.2 mag, (ii) find the median, and (iii) keeping data within a brightness interval ± 0.2 mag from median. This procedure reduced our dataset by only 2.4%.

3.2 NSVS data

The Northern Sky Variability Survey (NSVS) is a temporal record of the sky over the optical magnitude range from 8 to 15.5. It was conducted by the first-generation Robotic Optical Transient Search Experiment (ROTSE-I), using a robotic system of four co-mounted unfiltered telephoto lenses equipped with CCD cameras. The survey was conducted from Los Alamos, New Mexico, and primarily covers the entire northern sky (Woźniak et al. 2004). The NSVS contains light curves for approximately 14 million objects with a 1 yr baseline and typically 100–500 measurements per object. The NSVS public data release is available through a dedicated webpage¹.

We refer to the NSVS data as “Season 0” (in Tables 3, and 4). We have to note that for HD 31281 and HD 283572 no NSVS data are available. The mean cadence of observations of NSVS data was only ~ 0.6 d. Because of few data points (~ 105 per star) and the fact that the NSVS data observed usually only a single point per night, we have opted to not remove any of them.

To be able to analyse the NSVS data together with the SuperWASP data, we have made a simple linear transformation in magnitudes. For each target star we have found the mean magnitude (m_S) from the whole pre-cleaned SuperWASP dataset. Then we have computed the mean magnitude (m_N) of the corresponding NSVS dataset. All the NSVS data were shifted by $m_N - m_S$. We are interested mainly in temporal position of extremes in the light curves and the possible scaling of the amplitude of the NSVS light curve is of little concern.

3.3 Kepler *K2* data

The *Kepler Mission* was launched on 2009 March 6. Although it was designed primarily to detect variable stars and find transiting exoplanets (Borucki et al. 2010), the mission also provided exceptionally high photometric performance for all stars inside its field of view (FOV). The original FOV

¹ <http://skydot.lanl.gov/nsvs/nsvs.php>

Table 3. Observing seasons break-up for the NSVS ($\equiv 0$) and SuperWASP data. Not all of the target stars were observed in all seasons. When using the whole dataset, we referred to the one named Σ . Additional observation by the *K2 Mission* were used as C4 and C13.

Season	Start	End	Dur. [d]
0	1999-08-06	2000-03-26	233
1	2004-07-29	2004-09-30	63
2	2006-09-17	2007-02-27	163
3	2008-01-25	2008-02-06	12
4	2008-10-13	2009-03-07	145
5	2009-08-12	2010-03-26	226
6	2010-08-27	2011-02-16	173
7	2011-09-24	2012-01-30	128
Σ	1999-08-06	2012-01-30	4560
C4	2015-02-08	2015-04-20	70
C13	2017-03-08	2017-05-27	80

was centred in the constellation Cygnus (Koch et al. 2010). After pointing and stability problems, the mission was extended to other fields along the ecliptic and dubbed *K2* (Howell et al. 2014). The estimated photometric precision is down to 400 ppm for stars with $V = 12$ mag (Howell et al. 2014). In the original proposal, the Taurus-Auriga cluster was planned for the C4 (2015 February–April, centred at R.A. = 03 56 18, DEC = +18 39 38) observational campaign. After the next extension, another field C13 (2017 March–May, centred at R.A. = 04 51 11, DEC = +20 47 11) was added².

Since we were unable to find reliable periods in some observational seasons for several targets, we wanted to confirm and refine the values by using the *Kepler* data. With the exception of TTS20, we have only one season of data per target available. The data were observed with a 30-minute-long exposure in the *Kepler* magnitude (white light). Since we were interested in periods longer than 0.2 day, we have used the provided PDC SAP flux directly corrected for most systematics by the data conditioning pipeline (Stumpe et al. 2012).

Because we have used *Kepler* data in a separate analysis, we did not need to transform the measured fluxes or the *Kepler* magnitudes.

4 PERIOD SEARCH

The majority (70% of observation nights) of all photometric data was provided from the SuperWASP archive (seasons 1–7) with mean cadence of 80 seconds. We have also added ground-based data from the NSVS (season 0) with a mean cadence over the whole dataset of 0.6 days. However, if there were more than one data points per observation night the mean cadence was about 45 minutes. Ten out of the twenty targets were observed in campaign fields of *K2 Mission* with a 30-minute long cadence. All of the chosen datasets are usable for period searches in the regime of several days. Although the NSVS dataset has the lowest cadence, it has the

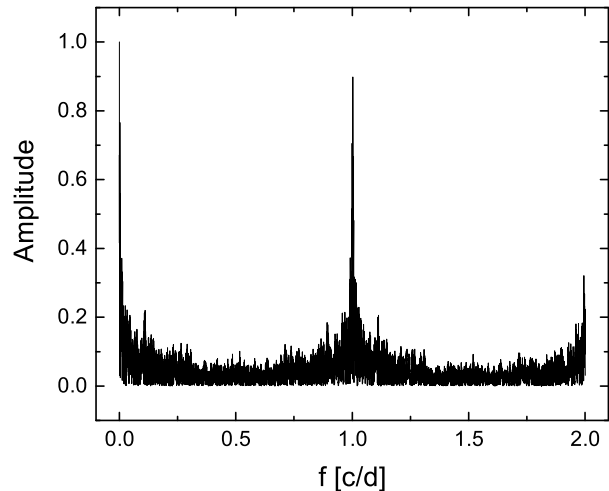


Figure 2. The spectral window of the SuperWASP dataset (Σ) constructed for HD 285957. This target has the most observation nights available.

longest duration of a single season (see Table 3). The previously identified rotational periods were in the range of 0.7 to 3.33 days (Table 1).

We chose to investigate the individual observing seasons separately to account for possible period changes between them. The problematic season 3 (with only twelve nights of observation) and season 4 (usually with very few data) were investigated only when non-trivial Fourier plots were found. Finally, we have also performed a period search on the combined dataset (Σ), constituted from seasons 0–7. The NSVS data were transformed before adding them into the combined dataset (see section 3.2). The phased light curves presented in Figures A4 and A5 were constructed using all available ground-based pre-cleaned data points (see section 3.1) and folded on the period corresponding to the most prominent frequency found in the Σ dataset.

Kepler datasets (seasons C4 and C13) were investigated separately from the ground-based data. Except for star HD 285778, only one season of *K2* data was available per object. In the single special case we have conducted the period search on both C4 and C13 data separately.

4.1 Ground-based data

The period analysis was performed using the Date Compensated Discrete Fourier Transform algorithm (DC DFT) of Ferraz-Mello (1981). The advantage of this method is that it compensates for gaps within the dataset using weighting, alias discrimination and harmonic frequency filtering.

The starting frequency was chosen based on the length of the combined dataset to be 0.00011 c/d. This corresponds roughly to periods between 0.2 and 9000 days. The step in frequency was set to average 0.0001 c/d. Because the NSVS data provided only handful of points per night, we have set our maximum frequency to 2 cycles per day (c/d) and all Fourier plots (Figures A1 and A2) are calculated up to this frequency.

We have used two software packages that utilize DC DFT for the search of periods in our datasets.

The initial analysis was done with the *VStar* package

² <https://keplerscience.arc.nasa.gov/k2-fields.html>

developed by the American Association of Variable Star Observers (AAVSO). This tool allowed us to search for all significant periods (intrinsic or harmonic) and order them with decreasing power in their Fourier spectrum. It also enabled visual checks to affirm the periodicity by constructing phase plots for any given frequency (period).

A subsequent analysis was done using the **Period04** software (Lenz & Breger 2004) with the same frequency range and frequency step for DC DFT. The code searches only for the most prominent frequency in the Fourier spectrum. The list of suspected frequencies (periods) from previous investigation using the **VStar** package were refined using **Period04**. The advantage of **Period04** was that noise peaks were less likely to be included in the final list of identified frequencies (Breger et al. 2011).

To further discern the intrinsic periods from aliases, we have constructed the spectral window of each dataset (e.g. see Figure 2). The most significant period peak was convolved with the spectral window and subtracted from the previously computed period spectrum (i.e. the corresponding frequency was pre-whitened for the next analysis).

The result was visually inspected. If the RMS of residuals was too large, the peak was discarded from the subsequent analysis. Frequency peaks with a signal-to-noise ratio > 2.0 were considered for further analysis. The procedure was repeated until the amplitude of the most significant peak left was $\leq 10\%$ of the original most significant period. Remaining frequencies were included in Table 4.

After periodicity has been identified, we have performed a Marquardt algorithm-based non-linear least-squares fitting (Bevington & Robinson 1993) simultaneously with all the identified frequencies, resulting in an adjusted set of parameters (i.e. frequencies, amplitudes and phases).

The least-squares fit by **Period04** also provided an error matrix, but the derived uncertainties only estimate the consistency of fit. The **Period04** package has a tool to compute more realistic uncertainties using Monte-Carlo simulations, which we have used with the default values.

The detected periodic signals were subtracted out and the remaining data points were randomly rearranged with the original timestamps preserved. A pseudo-random (based on the on-board computer time) Gaussian noise with a standard deviation of 0.1 was added to the magnitudes predicted by the last fit. For each optimization a set of total 100 test time strings was generated. The identification of peaks and least-square fit to the light curve was carried out for each of the simulated time strings. The uncertainties were calculated on the distribution of fit parameters (Lenz & Breger 2005).

4.2 *Kepler* data

The period analysis was performed separately from the ground-based data. However, the same frequency domain (0.00011–2 c/d) was searched with a step of $\Delta f = 0.0001$ c/d. The mean data error was only 26 ppm. Combined with the 30-minute cadence and almost uninterrupted 70–80 days of observation, the resulting Fourier plots (Figure A3) are without much noise and period peaks are easily distinguishable. The peaks of most the significant periods in the regime of several days are corresponding to intrinsic

changes of the brightness and no spectral window aliases were expected above the frequency of $\sim 1/80 = 0.0125$ c/d.

The resulting most significant periods are presented in Table 5. We have compared the periods found from the *Kepler* data with the mean periods found in our previous analysis of SuperWASP and NSVS data, as well as with the values found in the literature.

The period analysis of *Kepler* data yielded similar periods to those obtained from the ground-based data only. The mean difference was of the order of ~ 0.1 days. In comparison to Table 4, the mean uncertainties in periods were smaller because of clear and prominent peaks in Fourier plots. Several dubious periods (e.g. for BD+19 656) found in some observing seasons in SuperWASP data were also discovered with smaller amplitudes, and corresponded to a near 1:2 period ratio with the most prominent period. This indicates that spots areas are distributed along the length of the equator. For stars HD 283782 and HD 31281 we were able to find first reliable periods only from the *Kepler* data. Objects with different period estimates are discussed further in Section 4.3 below.

In addition to period determination, we have looked at the possible evolution of the period during the ~ 80 -day long *Kepler* observation. We have used the Wavelet Z-transform (WWZ) algorithm by Foster (1996), provided within the **VStar** package. The algorithm can achieve resolution in both frequency and time for unevenly spaced data. The wavelet was a sinusoidal wave shifted with a constant term. A sliding window of a constant width (in time) moved across the data.

The highest weight was applied to the data points closest to the centre of the window. The output was a relation between the signal power (Z value) as function of time and frequency. We were interested in tracking the maximum Z value for any given time. The frequency corresponding to the maximum Z value was interpreted as $1/P$ (see e.g. Figure 4).

To cover the period range from all investigated targets, we have run the wavelet analysis for periods from 0.5 to 4.0 days with the light curve separated into 50 time bins. The step in period was set to $\Delta P = 0.01$ days (half of the cadence interval) and the so-called decay parameter was fixed at the default value 0.001. The maximum Z-values for individual time bins were plotted along with the corresponding semi-amplitudes of the light curve (see Figure A8). Since we had only the total flux in the *Kepler* passband, we have expressed the amplitude of the light curve only as a ratio and not in magnitudes.

We have also constructed a simple spot model to compute artificial light curves with emerging and disappearing spots. The spherical stellar surface was covered with 360×181 mesh in longitude and latitude. Flux was calculated for each grid point taking into account the size of the local grid, the presence of spots and visibility for the observer. A linear limb-darkening law was used. Spots were placed at arbitrary longitudes (on the equator) and revolved with the rotation period. The inclination of stellar rotation axis was zero and a rigid rotation was assumed. We were able to set the time of appearance and disappearance of individual spots.

We have generated long (duration $> 10P_{\text{rot}}$) light curves for several scenarios and applied both period and wavelet

analyses using the **VStar** package. Results of two different setups are presented in Figure 3.

Table 4. Results of period analysis for all target objects. The prominent periods for the same object listed by decreasing power. Seasons without any usable data are marked as “–”. The last column lists periods obtained from the literature (see Table 1) “?” denotes uncertain values. Values in brackets “(”, “)” are not considered as the intrinsic period.

Object	Most prominent period [d] in seasons								P_{mean} [d] Σ	A_{mean} [mag]	P_{lit} [d]
	0	1	2	3	4	5	6	7			
HD 285281	1.1697(37)	1.1689(29)	1.1705(39)	–	–	1.1706(44)	1.1722(36)	1.1716(12)	1.1711(37)	0.0413(51)	1.1683
BD+19 656	⟨1.0041(285)⟩	⟨1.4421(207)⟩	2.9104(353)	–	–	2.8885(59)	2.8869(289)	⟨1.4611(188)⟩	2.8849(51)	0.0080(3)	2.8600 (0.7410)
HD 284135	⟨0.9986(204)⟩	0.8181(144)	0.8183(69)	–	–	0.8175(325)	0.9175(121)	0.8245(67)	0.8179(58)	0.0106(20)	0.8160
HD 284149	1.0309(316)	1.0353(192)	1.0534(224)	–	–	1.0473(268)	1.0419(362)	1.0684(84)	1.0712(7)	0.0084(3)	1.0790
HD 281691	2.6596(171)	2.6511(77)	2.6610(294)	–	–	2.6274(339)	2.6589(328)	2.6226(157)	2.6267(237)	0.0177(17)	2.74?
HD 284266	1.8086(185)	1.8218(237)	1.8087(183)	–	–	⟨0.9016(133)⟩	1.8396(24)	1.8403(88)	1.8433(10)	0.0315(4)	1.83
HD 284503	0.5166(183)	0.7396(148)	0.7369(227)	–	–	0.7308(78)	0.7363(64)	0.7369(58)	0.7370(3)	0.0267(25)	0.736
HD 284496	2.7248(211)	2.7056(205)	2.7390(336)	–	–	2.6617(266)	2.7556(882)	2.6846(763)	2.6880(195)	0.0486(23)	2.71
HD 285840	1.5562(177)	–	⟨1.2241(3247)⟩	1.5323(1134)	–	1.5470(395)	1.5751(306)	1.5538(224)	1.5476(67)	0.0315(26)	1.55
HD 285957	3.0874(294)	–	3.0497(330)	⟨4.1736(5446)⟩	3.0798(236)	3.0950(534)	3.0619(383)	3.0931(336)	3.0546(255)	0.0251(15)	3.07
HD 283798	0.9868(107)	⟨0.8906(1934)⟩	0.9861(92)	–	–	⟨0.9957(340)⟩	0.9890(154)	0.9860(93)	0.9872(33)	0.0159(5)	0.6?
HD 283782	⟨1.0016(91)⟩	⟨1.0413(319)⟩	⟨0.8706(1873)⟩	–	–	⟨1.0589(872)⟩	⟨0.8716(1333)⟩	⟨0.8684(1139)⟩	⟨0.8704(1106)⟩	0.0081(26)	?
HD 30171	⟨0.9956(2272)⟩	–	1.1053(873)	1.1013(1057)	1.1106(141) (0.5254(32))	1.1055(210)	1.1101(141)	1.1062(164)	1.1058(33)	0.0272(13)	1.104
HD 31281	–	–	⟨0.7920(1100)⟩	⟨0.7960(1181)⟩	–	–	–	–	⟨0.7913(15)⟩	0.0098(12)	?
HD 286179	3.2573(627)	–	3.1486(1914)	⟨0.9272(621)⟩	3.1260(401)	3.1476(501)	3.3201(199)	–	3.1397(221)	0.0294(13)	3.33
HD 286178	⟨0.7490(15)⟩ 2.0442(125)	–	⟨1.6958(281)⟩ 2.4242(551)	⟨0.7759(1023)⟩ 2.0198(210)	2.3680(399) ⟨1.7013(220)⟩	⟨1.6981(329)⟩ 2.4155(642)	⟨1.6990(387)⟩ 2.4155(735)	–	⟨1.7001(81)⟩ 2.4125(164)	0.0231(37) 0.0227(34)	2.39
HD 283447	3.0883(239)	3.0741(1071)	3.0912(268)	–	–	3.0628(141)	–	3.0826(374)	3.0836(210)	0.0695(24)	51
HD 283572	–	1.5392(175)	1.5475(227)	–	–	⟨1.4077(829)⟩	1.5823(544)	1.5470(208)	1.5462(38)	0.0386(22)	1.529
HD 285778	⟨0.9951(333)⟩	–	⟨1.2602(194)⟩	⟨0.9801(879)⟩	2.7293(1542)	2.7412(541)	2.7360(1030)	2.7308(759)	2.7361(204)	0.0132(32)	2.734
HD 283518	1.8723(26) (0.9362(27))	1.8716(63) ⟨0.9358(35)⟩	1.8713(645) ⟨0.9356(151)⟩	–	–	1.8734(641) ⟨0.9367(239)⟩	⟨0.9361(118)⟩	1.8702(377) ⟨0.9351(92)⟩	1.8706(14)	0.0491(18)	1.87

Note: Uncertain periods are further discussed in section 4.3.

Table 5. Results of period analysis for objects with available *Kepler* data. Periods, P_{Kepler} , are ordered by decreasing power of the corresponding peak. Values in brackets “(”, “)” are not considered as the intrinsic period. Comparison with previously determined periods (P_{lit}) and periods based on SuperWASP data (P_{mean}) are also shown.

Object	P_{lit} [d]	P_{mean} [d]	P_{Kepler} [d]	Field
BD+19 656	2.86	2.8849(51)	2.8489(8) (1.4467(4))*	C4
HD 284496	2.71	2.6880(195)	2.7738(8) (2.6525(6))	C13
HD 285840	1.55	1.5476(67)	1.5463(2) (0.7735(1))*	C13
HD 285957	3.07	3.0546(255)	3.0863(10) (1.5311(2))*	C13
HD 283798	0.6?	0.9872(33)	0.9831(2) (0.9658(2))	C13
HD 283782	?	(0.8704(1106))	2.0181(4)	C13
HD 31281	?	(0.7913(15))	0.6771(1) (0.7999(1))	C13
HD 286179	3.33	3.1397(221)	3.1249(20) (1.5647(5))*	C13
HD 286178	2.39	1.7001(81)	1.7027(6) (2.3562(11))* (1.1813(3))!	C13
HD 285778	2.734	2.7361(204)	2.8554(17) (1.3717(4))* 2.7510(15)	C4 C13

Note: Periods marked with “*” are close to 1:2 ratio with the more prominent period. See the discussion in text for details on special cases marked with “!”.

One typical situation similar to our Sun is when a new spot emerges on the stellar limb while the original spot is still present. After several days, the older spot declines and disappears while the new one is still present (see the left panel in Figure 3). The Fourier analysis will find only a “median” period P_1 (of periods in the individual spot evolution time step).

If two spotted regions were placed almost on the opposite sides of the stellar surface a sudden change of period is encountered (see the right panel in Figure 3). Fourier analysis finds two most significant periods (P_1 , P_2). The intrinsic rotation period was closer to the longer period found by Fourier analysis. This means that we have to be cautious about interpreting most significant periods of *Kepler* targets. The evolution of rotation period and its amplitude during ~ 80 days for all target stars is shown in Figure A8.

4.3 Discussion on individual targets

The adopted periods we discuss here stem from the period analysis on the whole ground-based dataset (Σ). We include a note if we have found different non-harmonic periods in a

singular observing seasons (see Table 4). Wherever possible, we have preferred the period found in the *Kepler* dataset (Table 5). Fourier plots and wavelet analysis of period evolution can be found in the appendix (Figures A3 and A8).

All periods found for the objects in our sample are interpreted as rotation periods due to magnetic cool spots on the surface of the star. There are other possible sources of periodic signals in T Tauri stars, e.g. hot spots in the circumstellar disk, and/or obscuration with material at the inner disk edge. However, studies using the IRAS (Strom et al. 1989) and Spitzer (Padgett et al. 2006) telescopes found that such disks are rare among WTTS. Hartmann et al. (2005) found that in the Taurus-Auriga region, the CTTS are clearly separated from WTTS based on the infrared colour excess. So far there have been no disks detected around stars in our sample.

For star **BD+19 656** we have found two periods in our ground-based data analysed season-wise. However, the main period was found when analysing the whole data set and also the *K2* data to be ~ 2.85 days, which corresponds to the value previously reported in literature (see e.g. Grankin 2013). Based on the modelled period evolution, the intrinsic rotation period may be shorter. We have visually examined the *Kepler* light curve phased with both prominent test periods separately (see Figure A7) and decided to adopt the period $P = 2.8489$ days.

Periods of **HD 284496** in different observational seasons ranged from ~ 2.66 to ~ 2.76 days. These two limits were resolved as separate close peaks by the period analysis of *Kepler* data (see Figure A3). The most prominent period $P = 2.7738(8)$ days was found to be the central value of period changes during the C13 season, investigated by the wavelet analysis. Based on the modelled period evolution, the intrinsic rotation period may be shorter.

For stars **HD 285840** and **HD 285957** the period analysis of the ground-based data and *Kepler* data provided the same results. The outlier periods found in a single season do not have any physical meaning. Also, the wavelet analysis showed no significant changes (~ 0.02 days) over the range of 80 days. The second most significant period found in the *K2* data is in 1:2 ratio to the mean period. This could indicate that some of the larger spotted regions are located on the opposite sides of the stellar surface. However, the modelled period evolution showed no sudden change in period. This could be explained by e.g. the both spotted regions are present on the surface and small changes of period can be attributed to differential rotation of spots changing their latitude. However, by folding the *Kepler* light curve with longer and shorter test periods for both stars (see Figure A7), we have adopted the periods $P = 1.5463$ days and $P = 3.0863$ days for HD 285840 and HD 285957, respectively.

The star **HD 283798** was found to have a period of $P \sim 0.987$ days. However, the corresponding frequency ($f = 1.013$ c/d) was distinguished from the peak at $f = 1.0$ (see Figure A2) and with higher amplitude. This is an unfavourable case for ground-base observations and could be the main reason why the star had no published period in the literature. However, in the *K2* dataset we have found clear peaks at $P = 0.9831(2)$ and $P = 0.9658(2)$ days.

We have found a previously unpublished period $P = 0.87(11)$ days for **HD 283782**. However, in several observ-

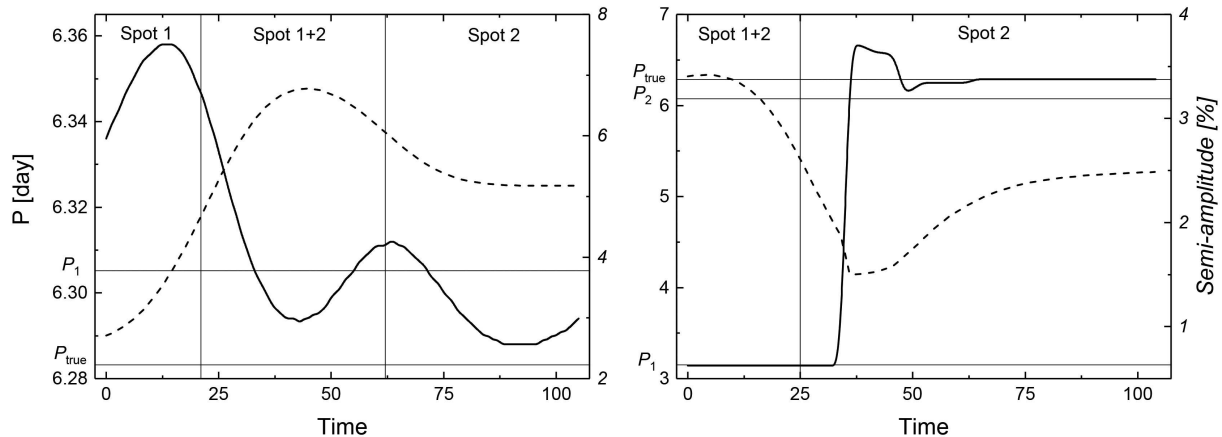


Figure 3. The evolution of period (solid line) and amplitude (dashed line) of the simple spot model light curve. The left panel shows the effect of a new randomly-placed spot and subsequent disappearance of the original spot. The right panel shows the effect of two spots placed on the opposite sides of the stellar surface with later disappearance of the original spot.

ing seasons we have detected periods close to one day. The Fourier plot (see Figure A2) was noisy with the mean SNR of 1.7. Because of large uncertainties and spurious periods, we have performed a separate period analysis on the *Kepler* data. We have found a different prominent peak at $P = 2.0181(4)$ days. The amplitude of the *Kepler* light curve is only about 0.25%. Other period peaks were present only in the red-noise region of the Fourier plot (see Figure A3). We have checked the data distribution in SuperWASP seasons 2, 6, and 7 (i.e. season which yielded the period ~ 0.87 day). The mean data cadence was ~ 72 seconds (~ 0.0008 day). We have investigated possible harmonic periods from the data sampling in these seasons. The length of uninterrupted observation of the star per night was found to be close to a normal distribution with the centre at ~ 4.6 hours (0.192 day). The corresponding frequency is above our threshold 4.8 c/d. A new period search extended up to 20 c/d was performed on the whole ground-base dataset. Interestingly, a new most prominent period of 0.317 days (3.1545 c/d) was found. The amplitude of frequency corresponding to period 0.192 day was less than 10% of the new most prominent period. We have not been able to link the periods 0.192 day, 0.317 day, or their harmonic multiples to any other period peak found in the Fourier plots for seasons 2, 6, and 7. However, the same period analysis on the *K2* data arrived to the most prominent period $P = 2.0181(4)$ days. Based on the modelled period evolution, the intrinsic rotation period may be shorter. We have adopted the *Kepler* period and consider all estimates from the ground-based data (in Table 4) to suffer from sampling effects. We have found first reliable period for **HD 283782** using the *Kepler* dataset. However, the evolution of this period computed by WWZ shows a decline from mean by ~ 0.2 days accompanied by a small drop in amplitude towards the end of continuous observation. A longer dataset would be needed to investigate further. Also, the mean period 2.02 days also provides problems for ground-based monitoring.

Analysing the dataset for **HD 31281** is not straightforward because it was observed only in seasons 2 and 3. The mean cadence was ~ 300 seconds spread on only 74 days of

observations. This resulted into a high amplitude of the diurnal frequency ($f = 1$) and also the red-noise contribution was substantial. The intrinsic frequency was found only as the third most significant one (see peaks marked with circles in Figure A2). Two of the most significant periods were pre-whitened leaving us with $P \sim 0.79$ day from the analysis of all data. The found amplitude was also small ~ 0.01 mag, which is probably the reason no period was published so far for this object. Fortunately, the *K2* data provided a mean period $P = 0.6771(1)$ day. The WWZ analysis showed two distinct periods present in the course of 80 days. A higher period (~ 0.8 day) was present for about 1/4 of the time interval. This corresponds to season 3 of SuperWASP data. The sudden change from 0.68 day to 0.79 day (lasting for about 20 days) can be interpreted with the emergence of another cool spotted region at the surface of the star together with the disappearance of a previous spotted region on the eastern limb of the star. If the change would be close to 50% we could argue that the spotted regions were almost at opposing sides. This was further accompanied by the change of amplitude of the light curve (see Figure 4). During the period-change event the amplitude curve has local minima, e.g. the percentage of surface covered with cool spots is higher at these times. We adopted the lower period as the intrinsic one. Based on the modelled period evolution, the intrinsic rotation period may be shorter.

The analysis of ground-based observation by SuperWASP and NSVS and *Kepler* data yielded the same result for star **HD 286179**, namely $P \sim 3.1397(21)$ days and $P \sim 3.1249(20)$ days, respectively. This value is smaller than previously reported by Bouvier et al. (1997) (3.33 days). A harmonic 1:2 period peak was also found in the C13 dataset. We have folded the *Kepler* light curve using both test periods (Figure A7). After visually inspecting the resulting phase curve, we have adopted the period $P = 3.1249$ days. The origin of period $P = 0.9272(621)$ days in Season 3 of SuperWASP is likely the result of a smaller number of data in comparison to other seasons.

When analysing data of **HD 286178** we found the most prominent period $P \sim 1.7$ days. This is the 1:2 harmonic of $P = 2.39$ days reported by Bouvier et al. (1997). However,

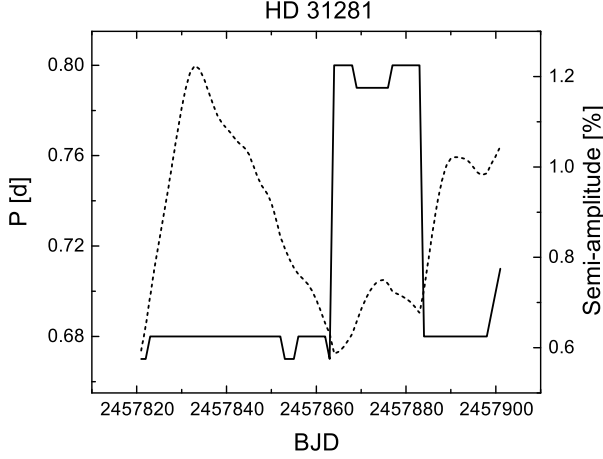


Figure 4. The evolution of period (solid line) and amplitude (dashed line) of the light curve of HD 31281 during the C4 campaign of *K2 Mission*. See text for details.

in our season 4 (2008–2009), we have found the most prominent period to be ~ 2.37 days. Data of Bouvier et al. (1997) were obtained during years 1994–1996. The change of the observed period can be explained, e.g. by emerging a previously unobserved area of photospheric spots. This would result in the shorter photometric period of ~ 1.7 days. We have repeated the period analysis with all the ground-based data binned to a single point per night spanning 12.5 years. The subsequent period analysis showed only one peak at $P \sim 2.4$ days. We are thus inclined to consider the rotation period to be close to this value. The *Kepler* dataset revealed prominent peaks at $P = 1.7027(6)$, $2.3562(11)$, and $1.1813(3)$ days (ordered with decreasing power). Also the wavelet analysis showed a sudden change of period from ~ 2.36 to ~ 1.70 days (see Figure 5). Based on the distance of 74.3 pc of HD 286178 (from Table 1) and stellar properties of $R = 1.04 R_{\odot}$, $L = 0.71 L_{\odot}$, and a reliable estimate of A_V we can write

$$R \sin i = (P_{\text{rot}} v \sin i) / 2\pi.$$

If we use the value of $v \sin i = 42 \text{ km.s}^{-1}$ by Wichmann et al. (2000), we obtain the values for $\sin i$. However, only for the period $P = 1.1813(3)$ days is $\sin i \leq 1$ which disallows the other periods $P = 1.7027(6)$ days and $2.3562(11)$ days from further analysis.

HD 283447 had a previously reported period $P \sim 51$ days (Welty 1995). The star was described as an SB2 system with K-type components. From the photometric point of view we have not found any signal corresponding to this period, i.e. the measured variations in flux are due to the changes on the visible photosphere. We have found a period $P = 3.0836(210)$ days with an amplitude $\sim 2\times$ the diurnal period.

HD 285778 was found to have a mean period of $\sim 2.7361(204)$ days from the ground-based data, which confirms the previously determined period by Grankin (2013). This object was also the only one from our sample to have two *Kepler* datasets available. In the C4 season an additional period was found. We have folded the data using both test periods (the result is shown in Figure A7). The descending slope between phases 0.2–0.8 folded with the pe-

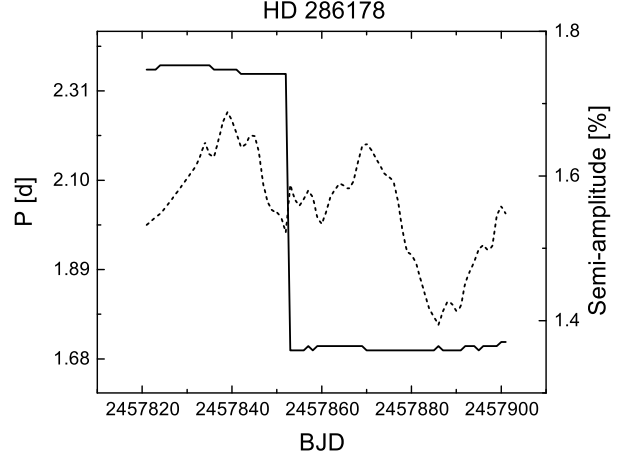


Figure 5. The evolution of period (solid line) and amplitude (dashed line) of the light curve of HD 286178 during the C13 campaign of *K2 Mission*. See text for details.

riod $P = 2.8554$ days is closer to the descending slope of the original light curve. The dubious period from the NSVS data $0.9951(333)$ days is most probably a window alias. The determination of a $0.9801(879)$ day period from season 3 was plagued by the low number of data points. In season 2, the period found was close to 1:2 and is caused by spots distributed by ~ 180 degrees on the surface of the star.

The most intriguing object is **HD 283518** (V410 Tau). This is a well-investigated star (see e.g. Stelzer et al. 2003; Grankin & Artemenko 2009). The phase light curve of the whole dataset (Σ) shows a clear frequency wave (see Figure 7) when folded with the most prominent period. The period analysis based on the whole dataset yielded two distinct peaks (Figure 6) at $P = 1.8758$ days, and $P = 0.9338$ days (ordered by their respective amplitude). We have to apply the DC DFT analysis for separate seasons (0–2 and 5–7, see Table 3 for dates of observations). Except for season 6, we have found the mean period ~ 1.87 day. To properly fit the light curve, we had to add the next harmonic frequency corresponding roughly to $P_2 \sim 0.936$ days. Phased light curves with a fit are presented in Figure 8. The added harmonic period can be interpreted as due to the presence of at least another spot located almost opposite the first spot area. Detailed spot configuration would need to be carried out by a Zeeman-Doppler imaging and surface inversion technique.

5 CONCLUSIONS

We have performed a thorough period analysis of twenty selected weak-line T Tauri stars based on the data available from the NSVS and the SuperWASP archive. For two objects (HD 283782 and HD 31281) we made the first estimate of the photometric period. Also we have found a more reliable period estimate for HD 283798. Period analysis based on all available data lead to the confirmation and update of periods previously published in literature in 15 cases (up to 10% difference).

The main advantage of these period estimates is that we have analysed a very long time interval (up to ~ 12.5 years).

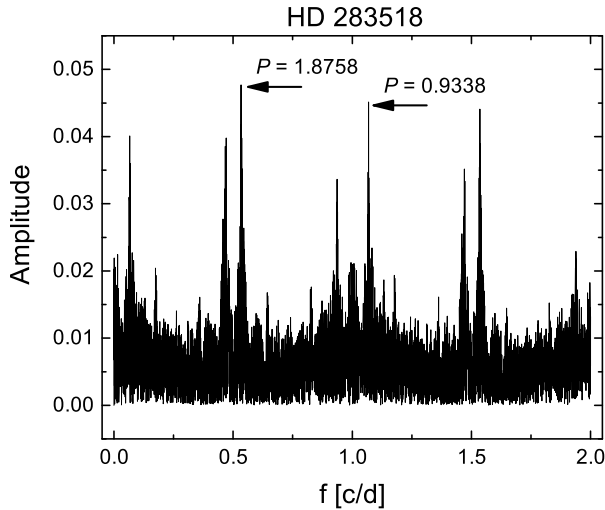


Figure 6. Fourier plot of the whole dataset (Σ) for HD 283518. Most prominent periods are marked. Other peaks are aliases from the spectral window.

Fortunately, our targets with dubious periods were also observed by the *K2 Mission*, which allowed us to distinguish the mean photometric periods from their harmonic components. We also have performed wavelet analysis for our stars observed by *Kepler* and searched for period evolution. The sudden change of period in several targets can be explained by the emergence of another photospheric spot which remained visible for several days.

We have constructed a simple spot model with the possibility of adding and removing spots to compute long artificial light curves. After that, period search and wavelet analysis were applied. We found that: (i) Fourier analysis found only a median period, but WWZ converged on the intrinsic rotational period, (ii) additional spots increased the amplitude and the most significant Fourier period of the light curve, (iii) period evolution was gradual if spots were close to each other, (iv) spots placed almost on the opposite sides of stellar disk generated a rapid change between P_{rot} and $P_{\text{rot}}/2$.

Using WWZ to investigate the period evolution can place further limits on the possible rotation period. A full model could deal with unknown inclination of the stellar rotational axis, differential rotation and spot migration. A light curve with very good sampling and long temporal duration is needed for such model.

The light curves of HD 283518 (V410 Tau) were analyzed separately for six individual observing seasons. The comparison of our study with past data hinted that the evolution of light curve variations caused by changes in the distribution of cool photospheric spots may be the result of a ~ 15 -year long cycle similar to the 11-year cycle of the Sun.

The evolutionary status of our targets was checked using accurate parallaxes and mean stellar parameters from the literature and calibrations of the Strömgren-Crawford *uvby β* photometric system. Thanks to the already published *Gaia* DR2 data, the luminosities are already very accurate with the largest uncertainty contribution coming from the a-priori unknown reddening. Furthermore, the uncertainties of the effective temperatures prevent a suitable calibration

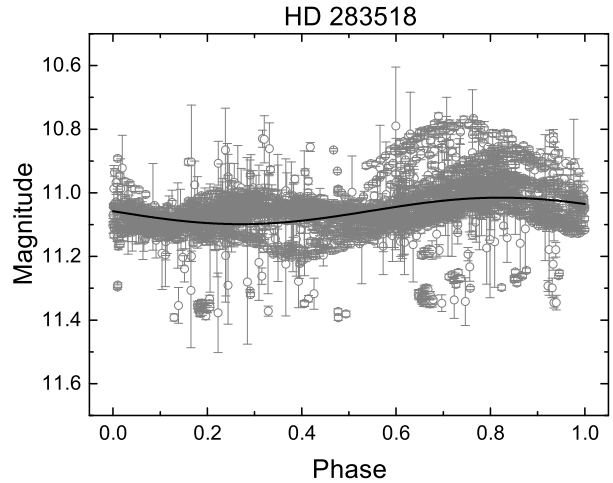


Figure 7. Light curve of all available photometry from SuperWASP and NSVS data for the HD 283518 folded with the mean period $P = 1.8706$ days.

of the age and mass to correlate these parameters with the rotational periods.

Therefore, we are continuing our investigation on selected targets with dedicated spectroscopic observations to provide accurate and homogeneous effective temperatures.

SUPPORTING INFORMATION

Additional Supporting Information may be found in the online version of this article:

Figures A1 and A2: Fourier plots of investigated targets from ground-based observations

Figure A3: Fourier plots of targets with available *Kepler* photometry

Figures A4 and A5: Light curves of investigated targets phase-folded with periods estimated from a single season

Figure A6: Light curves of targets observed by *Kepler*

Figure A7: Phased light curves of targets with more than one prominent period in the *Kepler* data

Figure A8: Evolution of period and amplitude of light curves of our *Kepler* targets

ACKNOWLEDGMENTS

This study has been supported by the projects VEGA 2/0143/14, VEGA 2/0031/18, APVV-15-0458 and 7AMB17AT030 (MŠMT). This article was created by the realisation of the project ITMS No.26220120029, based on the supporting operational Research and development program financed from the European Regional Development Fund. This work has made use of data from the European Space Agency (ESA) mission *Gaia* (<https://www.cosmos.esa.int/gaia>), processed by the *Gaia* Data Processing and Analysis Consortium (DPAC), <https://www.cosmos.esa.int/web/gaia/dpac/consortium>). Funding for the DPAC has been provided by national institutions, in particular the institutions participating in the *Gaia* Multilateral Agreement. This paper includes data collected by the *Kepler* mission. Funding for the

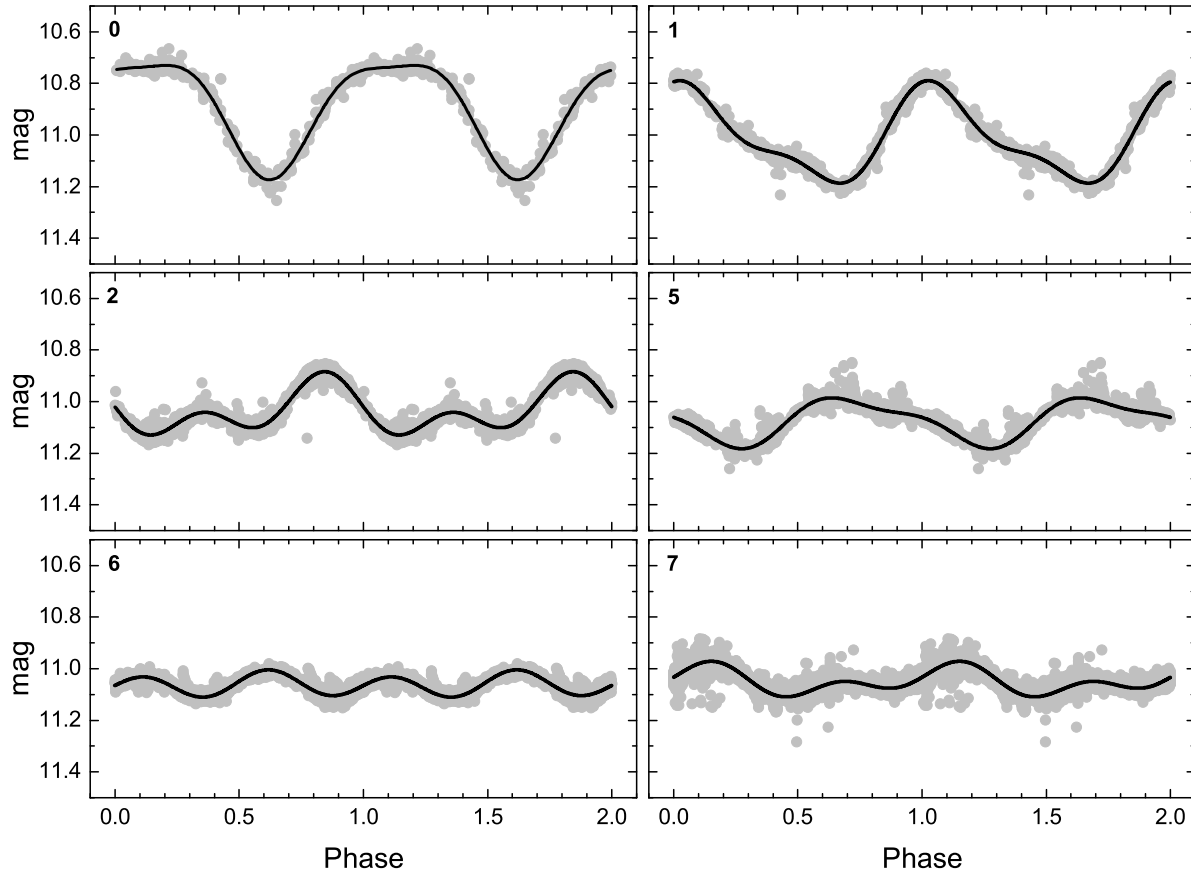


Figure 8. Evolution of the phased light curve of star HD 283518 in different observational seasons (panel number). The most dominant frequency in each season (see Table 4) was used to construct the phased light curve. The solid line represents a fit with the addition of the first harmonic frequency.

Kepler mission is provided by the NASA Science Mission directorate. Some/all of the data presented in this paper were obtained from the Mikulski Archive for Space Telescopes (MAST). STScI is operated by the Association of Universities for Research in Astronomy, Inc., under NASA contract NAS5-26555. Support for MAST for non-HST data is provided by the NASA Office of Space Science via grant NNX09AF08G and by other grants and contracts. This research was made possible through the use of the AAVSO Photometric All-Sky Survey (APASS), funded by the Robert Martin Ayers Sciences Fund. We thank the reviewer for his/her thorough review and highly appreciate the comments and suggestions, which significantly contributed to improving the quality of the publication.

REFERENCES

- Alves de Oliveira C., Casali M. 2008, *A&A*, 485, 155
 Ammons S.M., Robinson S.E., Strader J., et al. 2006, *ApJ*, 638, 1004
 Appenzeller I., Mundt R. 1989, *Astron. Astrophys. Rev.*, 1, 291
 Bertout C. 1989, *Ann. Rev. Astron. Astrophys.*, 27, 351
 Bevington P.R., Robinson D.K. 1993, in *Data Reduction and Error Analysis for the Physical Sciences 3rd ed.* (McGraw-Hill), 161
 Billot N., Morales-Calderón M., Stauffer J.R., et al. 2012, *ApJ*, 753, L35
 Bonavita M., Daemgen S., Desidera S., et al. 2014, *ApJL*, 791, 40
 Borucki W.J., Koch D., Basri G., et al. 2010, *Science*, 327, 977
 Bouvier J., Wichmann R., Grankin K., et al. 1997, *A&A*, 318, 495
 Breger M., Balona L., Lenz P., et al. 2011, *MNRAS*, 414, 1721
 Butters O.W., West R.G., Anderson D.R., et al. 2010, *A&A*, 520, 10
 Cody A.N., Stauffer J., Baglin A., et al. 2014, *AJ*, 147, 82
 Carpenter J.M., Hillenbrand L.A., Skrutskie M.F. 2001, *AJ*, 121, 3160
 Chavarría-K C., Terranegra L., Moreno-Corral M.A., de Lara E. 2000, *A&A Suppl.*, 145, 187
 Crawford D.L. 1975, *AJ*, 80, 955
 Daemgen S., Bonavita M., Jayawardhana R., et al. 2015, *ApJ*, 799, 155
 Davies C.L., Gregory S.G., Greaves J.S. 2014, *MNRAS*, 444, 1157
 D’Antona F., Mazitelli I. 1994, *ApJ Suppl.*, 90, 467
 Eiroa C., Oudmaijer R.D., Davies J.K., et al. 2002, *A&A*, 384, 1038
 Ferraz-Mello S. 1981, *AJ*, 86, 619

- Fernández M., Stelzer B., Henden A., et al. 2004, *A&A*, 427, 263
- Flaherty K.M., Muzerolle J., Rieke G., et al. 2012, *ApJ*, 748, 71
- Foster G. 1996, *AJ*, 112, 1709
- Gahm G.F., Gullbring E., Fischerstrom C., et al. 1993, *A&A Suppl.*, 100, 371
- Grankin K.N. 2013, *Astron. Letters*, 39, 251
- Grankin K.N., Artemenko S.A. 2009, *Inf. Bull. on Var. Stars*, No. 5907
- Grankin K.N., Artemenko S.A., Melnikov S.Y. 2007, *Inf. Bull. on Var. Stars*, No. 5752
- Grankin K.N., Bouvier J., Herbst W., Melnikov S.Yu. 2008, *A&A*, 479, 827
- Grankin K.N., Melnikov S.Y., Bouvier J., et al. 2007, *A&A*, 461, 183
- Hartmann L., Megeath S.T., Allen L., et al. 2005, *ApJ*, 629, 881
- Herbig G. 1977, *ApJ*, 214, 747
- Herbst W., Herbst D.K., Grossman E.J., Weinstein D. 1994, *AJ*, 108, 1906
- Herczeg G.J., Hillenbrand L.A. 2014, *ApJ*, 786, 97
- Høg E., Fabricius C., Makarov V.V., et al. 2000, *A&A*, 355, 27
- Holdsworth D.L., Smalley B., Gillon M., et al. 2014, *MNRAS*, 439, 2078
- Howell S.B., Sobek C., Haas M., et al. 2014, *PASP*, 126, 398
- Hussain G.A.J. 2012, *AN*, 333, 4
- Ibryamov S.I., Semkov E.H., Peneva S.P. 2015, *Publ. of the Astron. Soc. of Australia*, 32, e021
- Jensen E.L.N. 2001, *ASPC*, 244, 3
- Johns C.M., Basri G. 1995, *AJ*, 109, 2800
- Joy A.H. 1945, *ApJ*, 102, 168
- Koch D.G., Borucki W.J., Basri G., et al. 2010, *ApJL*, 713, 79
- Lago M.T.V.T., Gameiro J.F. 1998, *MNRAS*, 294, 272
- Lebzelter T., Heiter U., Abia C., et al. 2012, *A&A*, 547, A108
- Lenz P., Breger M. 2004, in *The A-Star Puzzle (IAU Symposium 224)*, ed. J. Zverko, J. Žižňovský, S.J. Adelman & W.W. Weiss (Cambridge University Press), 786
- Lenz P., Breger M. 2005, *Comm. in Asteroseismology*, 146, 53
- Lindgren L., Hernandez J., Bombrun A., et al. 2018, *A&A*, in print
- McGinnis P.T., Alencar S.H.P., Guimarães M.M., et al. 2015, *A&A*, 577, 11
- McDonald I., Zijlstra A.A., Watson R.A. 2017, *MNRAS*, 471, 770
- Meištas E., Straišys V. 1981, *Acta Astron.*, 31, 85
- Menard F., Bertout C. 1999, in *The Origin of Stars and Planetary Systems*, ed. C.J. Lada, & N.D. Kylafis (Kluwer Academic Publishers), 341
- Michalik D., Lindgren L., Hobbs D. 2015, *A&A*, 574, 115
- Napiwotzki R., Schoenberner D., Wenske V. 1993, *A&A*, 268, 653
- Padgett D., Koerner D., Wahhaj Z., et al. 2006, *ASPC*, 357, 97
- Palla F., Stahler S.W. 2002, *ApJ*, 581, 1194
- Patterer R.J., Ramsey L., Huenemoerder D.P., Welty A.D. 1993, *AJ*, 105, 1519
- Paunzen E. 2015, *A&A*, 580, A23
- Pecaut M.J., Mamajek, E.E. 2014, *ApJ Suppl.*, 208, 9
- Percy J.R., Esteves S., Glasheen J., et al. 2010, *J. of the American Assoc. of Var. Star Observers*, 38, 151
- Pollacco D.L., Skillen I., Collier Cameron A., et al. 2006, *PASP*, 118, 1407
- Pribulla T., Garai Z., Hambálek Ľ., et al. 2015, *AN*, 336, 682
- Rebull L.M., Padgett D.L., McCabe C.E., et al. 2014, *ApJ Suppl.*, 186, 259
- Rice J.B., Strassmeier K.G., Kopf M. 2011, *ApJ*, 728, 69
- Rice T.S., Wolk S.J., Aspin C. 2012, *ApJ*, 755, 65
- Rigon L., Scholz A., Anderson D., West R. 2017, *MNRAS*, 465, 3889R
- Schlafly E.F., Green G., Finkbeiner D.P., et al. 2014, *ApJ*, 789, 15
- Schuster W.J., Nissen P.E. 1989, *A&A*, 221, 65
- Siess L., Forestini M., Bertout C. 1997, *A&A*, 326, 1001
- Smalley B., Kurtz D.W., Smith A.M.S., et al. 2011, *A&A*, 535, A3
- Stauffer J., Cody A.M., McGinnis P., et al. 2015, *AJ*, 149, 130
- Stelzer B., Fernández M., Costa V.M., et al. 2003, *A&A*, 411, 517
- Strom K.M., Strom S.E., Edwards S., et al. 1989, *AJ*, 97, 1451
- Stumpe M.C., Smith J.C., Van Cleve J.E., et al. 2012, *PASP*, 124, 985
- Swenson F.J., Faulkner J., Rogers F.J., Iglesias C.A. 1994, *ApJ*, 425, 286
- Tognelli E., Prada Moroni P.G., Degl’Innocenti S. 2011, *A&A*, 533, A109
- Welty A.D. 1995, *AJ*, 110, 776
- Wichmann R., Torres G., Melo C.H.F., et al. 2000, *A&A*, 359, 181
- Woźniak P.R., Vestrand W.T., Akerlof C.W., et al. 2004, *AJ*, 127, 2436
- Wright N.J., Drake J.J., Mamajek E.E., Henry G.W. 2011, *ApJ*, 743, 48

This paper has been typeset from a \LaTeX file prepared by the author.

APPENDIX A: FOURIER PLOTS AND PHASED LIGHT CURVES OF TARGET STARS

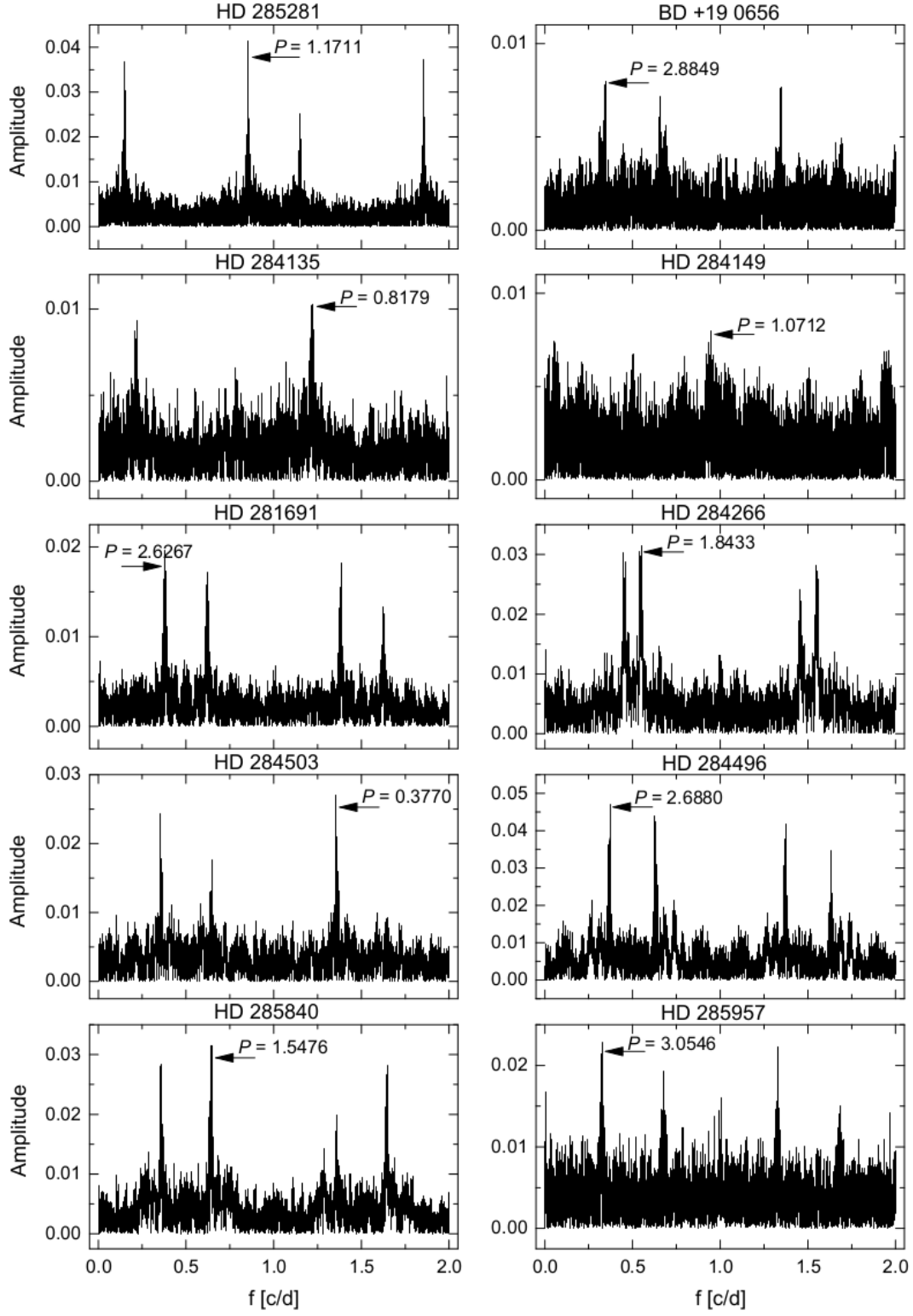


Figure A1. Fourier plots of investigated targets. Data from all seasons were used. Prominent frequencies are noted with an arrow. Details in text.

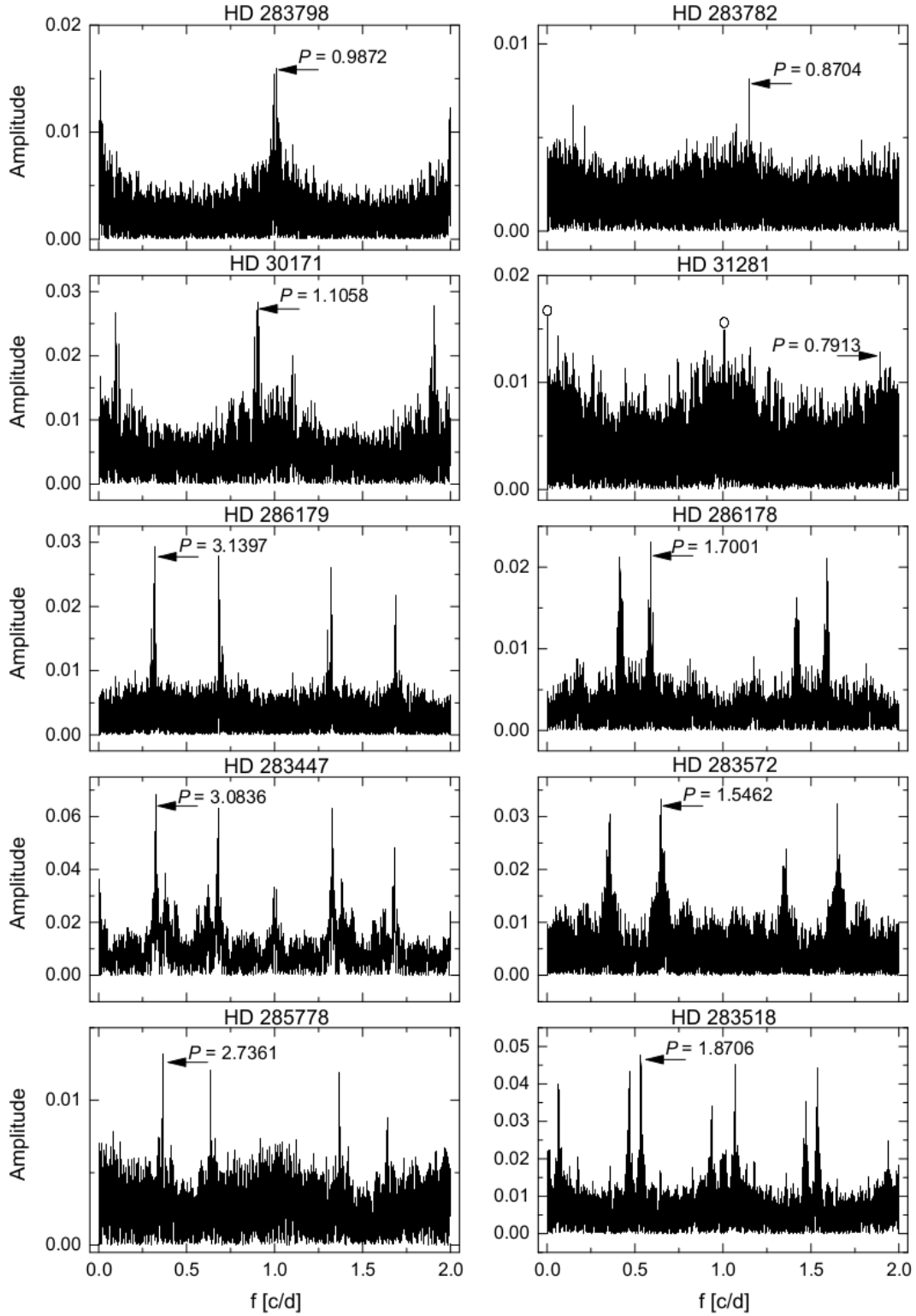


Figure A2. Fourier plots of investigated targets. Data from all seasons were used. Prominent frequencies are noted with an arrow. Details in text.

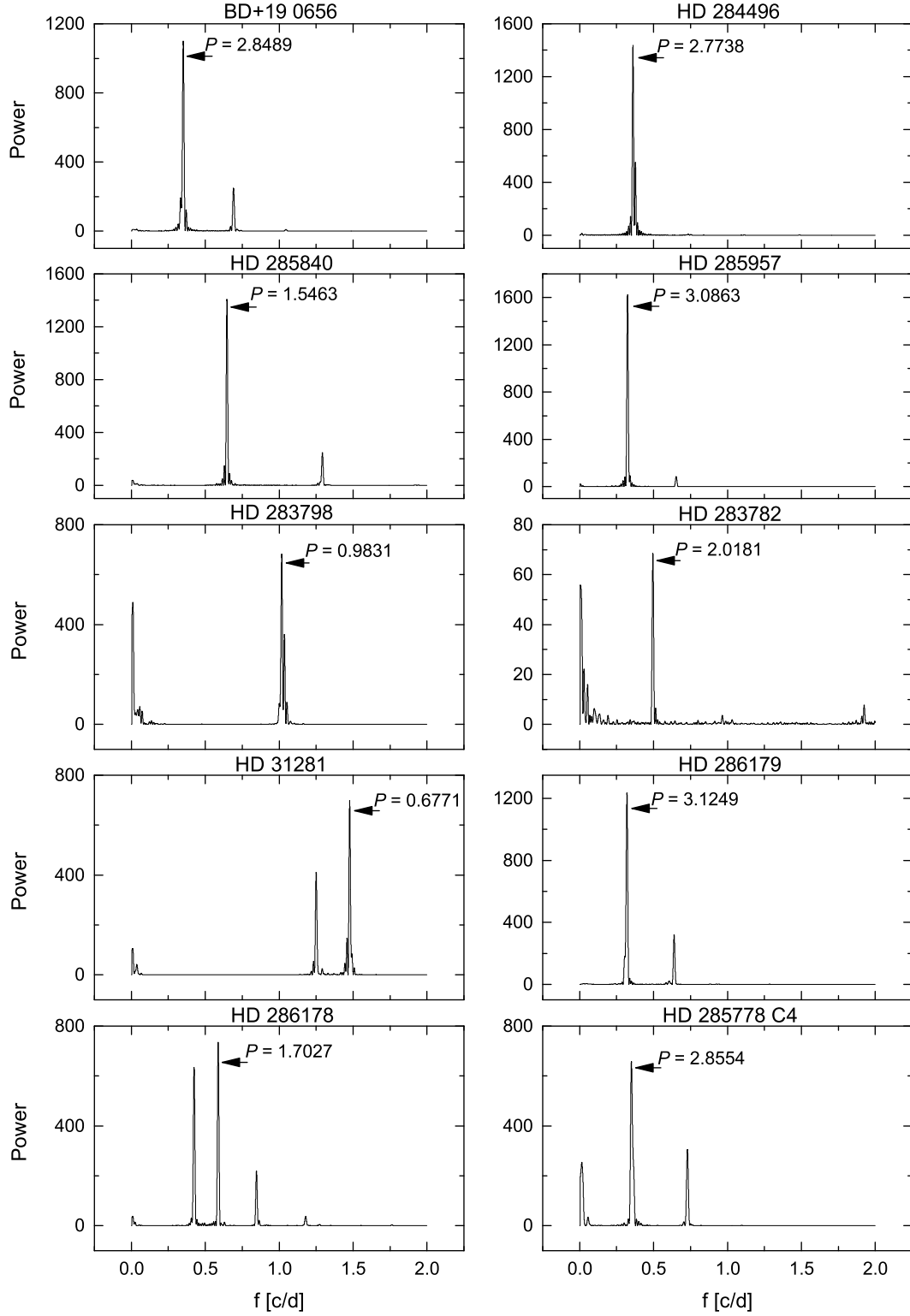


Figure A3. Fourier plots of targets with available *KEPLER* photometry. Prominent frequencies are noted with an arrow. Details in text.

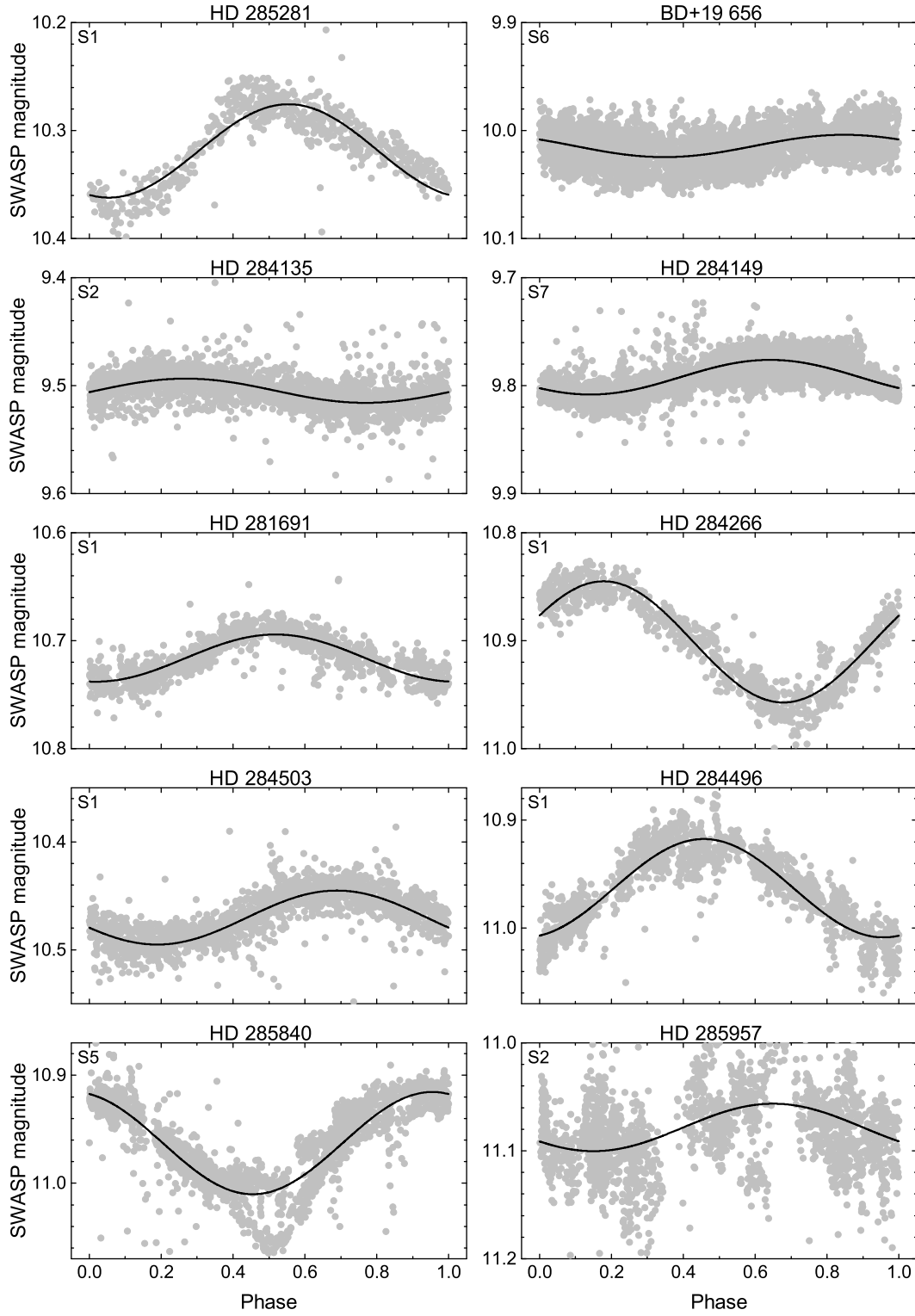


Figure A4. Light curves of investigated targets phase-folded with periods estimated from a single season - indicated by panel number. We have used only pre-cleaned data points (see Section 3.1).

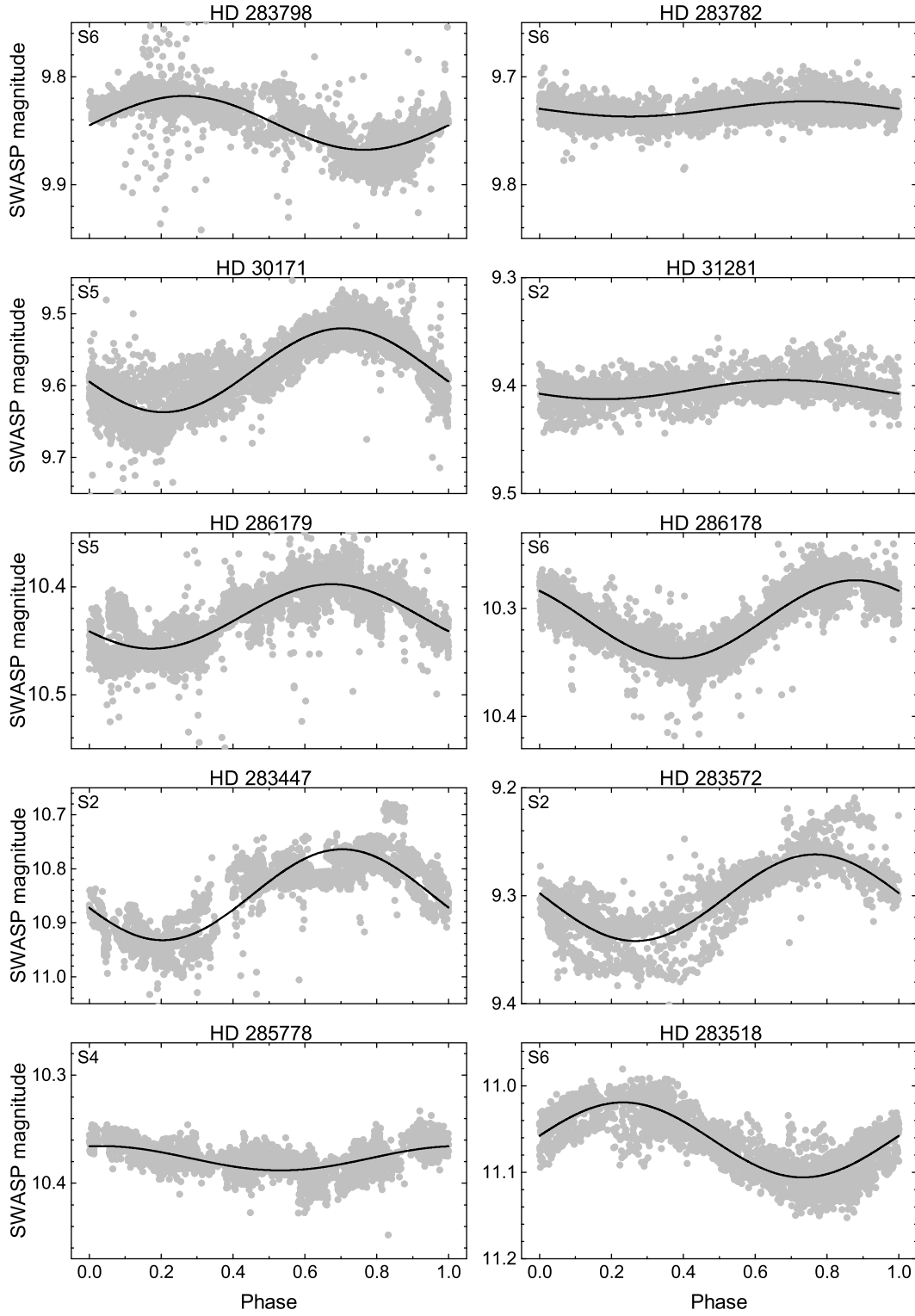


Figure A5. Light curves of investigated targets phase-folded with periods estimated from a single season - indicated by panel number. We have used only pre-cleaned data points (see Section 3.1).

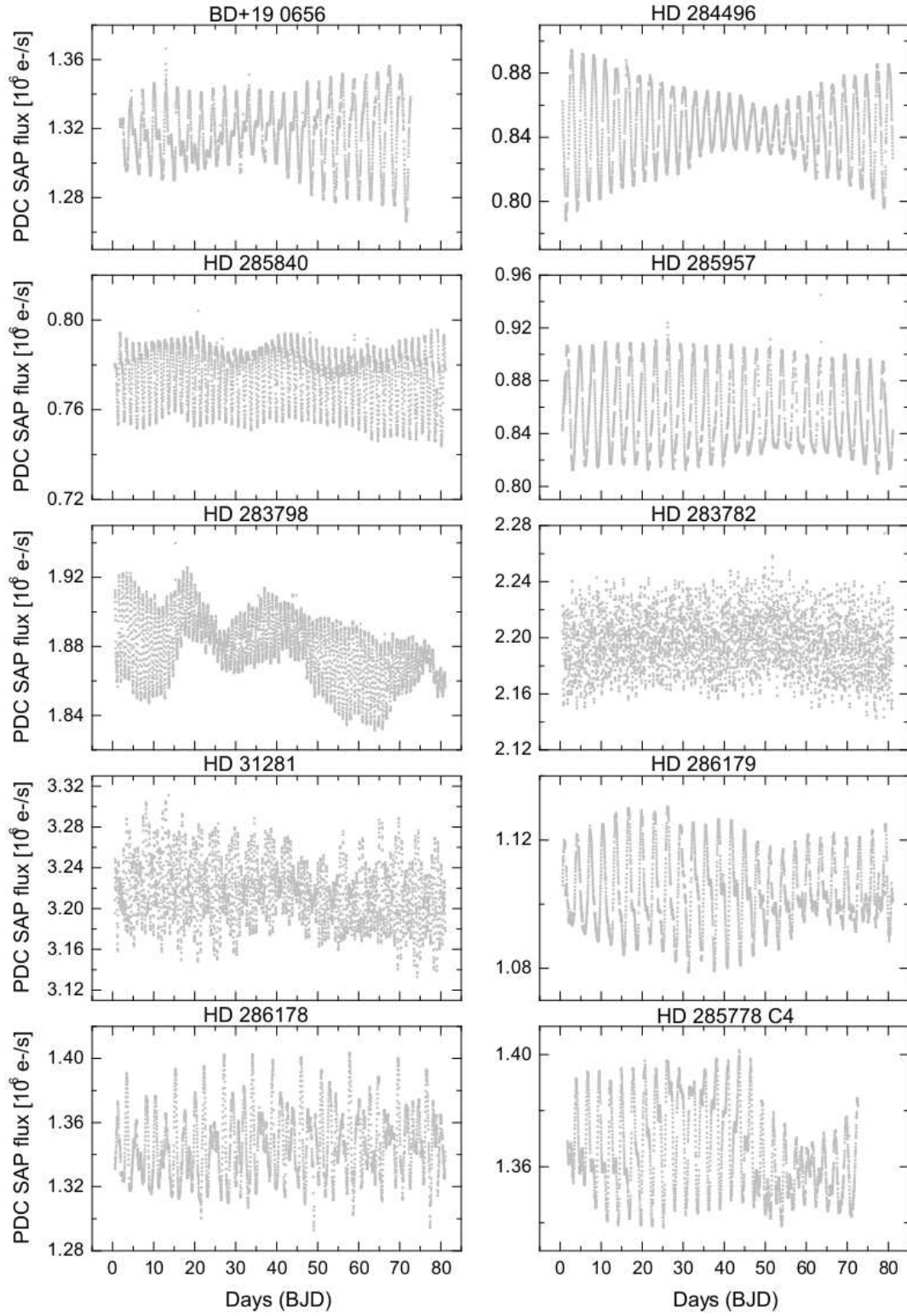


Figure A6. Light curves of targets observed by *Kepler*.

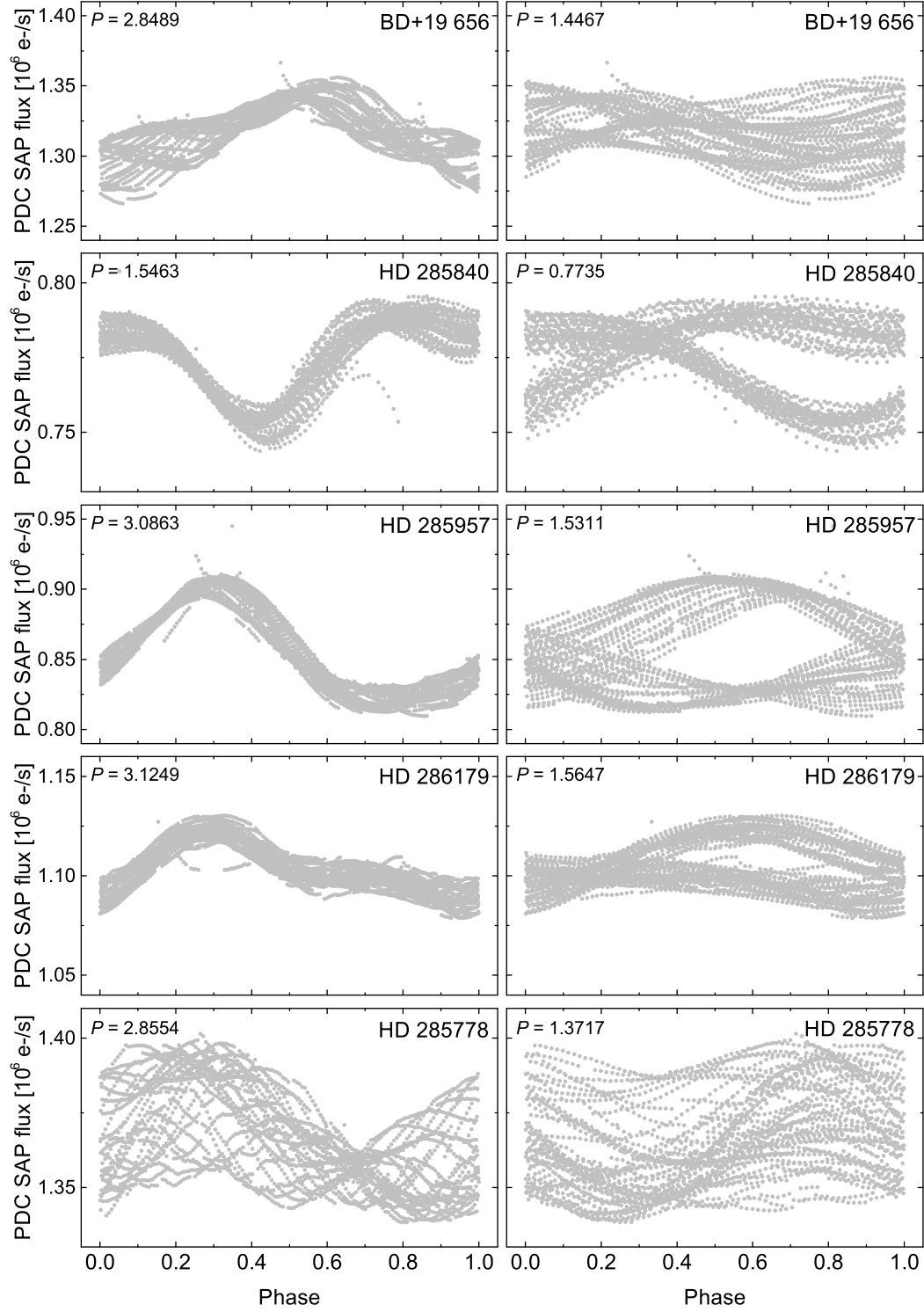


Figure A7. Phased light curves of several stars from our sample for which we have found more than one prominent period in the *Kepler* data. Data were folded with longer (left) and shorter (right) periods separately.

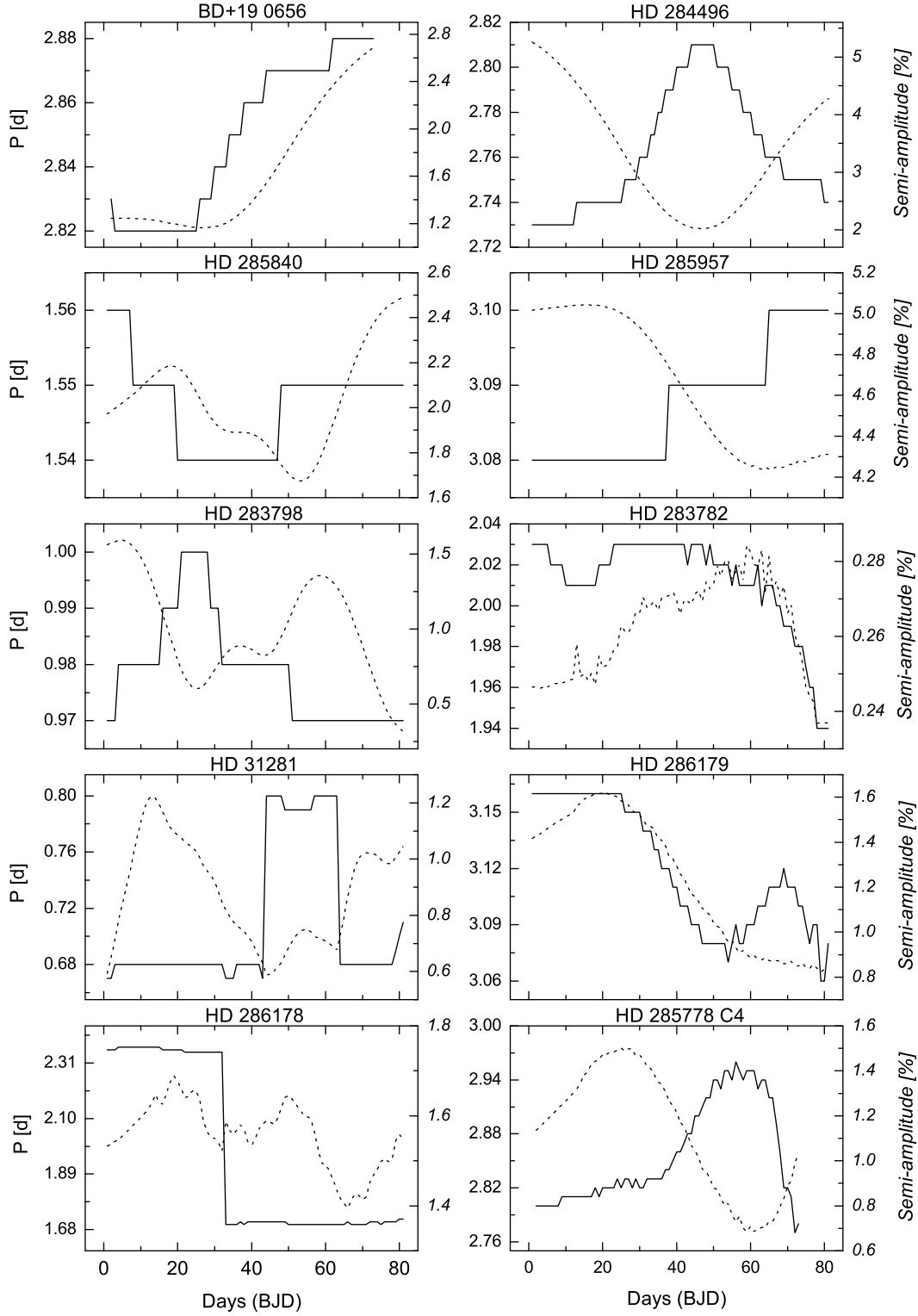


Figure A8. Evolution of dominant period (solid line) and amplitude (dashed line) of light curves of our *Kepler* targets in time. Stepping in periods is an artefact of frequency resolution.